POLITECNICO DI TORINO

Master's Degree in Aerospace Engineering

Politecnico di Torino

Master's Degree Thesis

Damping identification of a FOWT by means of a CFD-based simulation tool

Supervisors

Dr. Bruno PADUANO

Prof. Giovanni BRACCO

Ing. Oronzo DELL'EDERA

Candidate

Alessandro VITELLI

DECEMBER 2024

Summary

The focus of this thesis is to obtain the damping response for the structure of an offshore wind turbine subjected to different frequencies, consistent with the most probable sea conditions.

The simulations replicate a hypothetical testing facility, where a floating body is in controlled motion and the dynamic response of the system is analyzed, treating the water-body system as a mass-spring-damper.

The simulations are performed using the CFD software "Star CCM+", based on the RANS model. The results will be compared to a linear BEM model obtained from the software NEMOH, with corrections introduced to achieve higher-fidelity data, while maintaining the simplicity and low computational cost of the linear BEM simulations. All post-processing is carried out in Matlab, where the F(z) report is transformed from the time domain to the frequency domain using FFT, allowing the damping coefficient to be expressed as a function of frequency.

To test this approach, the first test case chosen is a simple sphere with a 1-meter radius. Once the procedure is validated, it's applied to a more realistic scenario, simulating a reference floating substructure, the UMaine VolturnUS-S.
Offshore wind energy production is a complex sector in steady growth, and a valid model that produces accurate results with a low computational cost is crucial in the initial stages of design.

Given the high computational cost of each simulation, testing every specific geometry would be impractical. The future goal, with sufficient data, is to propose a generic correction model for the BEM, at least for similar geometries.

Another important step would be validating the results of the numerical simulations with real experiments to ensure that the modeling accurately represents the phenomenon.

Sommario

L'obiettivo di questa tesi è ricavare lo smorzamento del sistema di una turbina eolica galleggiante a varie frequenze, coerenti con le più probabili condizioni del mare.

Le simulazioni replicano un ipotetico impianto di testing, dove una struttura galleggiante è in movimento controllato per studiarne la risposta dinamica, trattando il sistema acqua-corpo come un sistema massa-molla-smorzatore.

Le simulazioni sono eseguite utilizzando il software CFD "Star CCM+", basato sul modello RANS. I risultati verranno confrontati con un modello a potenziale BEM ottenuto dal software NEMOH, con l'obiettivo di introdurre correzioni per ottenere dati di maggiore precisione, mantenendo comunque la semplicità e il basso costo computazionale delle simulazioni BEM. Tutto il post-processing è effettuato in Matlab, dove il report F(z) viene trasformato dal dominio del tempo al dominio delle frequenze utilizzando l'FFT, permettendo di esprimere il coefficiente di smorzamento in funzione della frequenza.

Per testare questo approccio, il primo caso scelto è una semplice sfera con un raggio di 1 metro. Una volta collaudata la procedura, viene applicata a uno scenario più realistico, simulando una sottostruttura galleggiante di riferimento, l'UMaine VolturnUS-S. La produzione di energia eolica offshore è un settore complesso in crescita costante, e un modello valido che produca risultati accurati con un basso costo computazionale è cruciale nelle fasi iniziali del progetto.

Dato l'alto costo computazionale di ogni simulazione, testare ogni geometria specifica sarebbe impraticabile. L'obiettivo futuro, con dati sufficienti, è proporre un modello di correzione generico per il BEM, almeno per geometrie simili tra loro.

Un altro passo importante sarebbe la validazione dei risultati delle simulazioni numeriche con esperimenti reali per garantire che le simulazioni riproducano accuratamente il fenomeno reale.

Acknowledgements

RINGRAZIAMENTI

Dedico questo traguardo alla mia famiglia.
A mamma e papà, i miei meravigliosi punti di riferimento.
Ai nonni, che anche a centinaia di km di distanza mi hanno sorretto, con una preghierina prima di un esame o con un barattolo di sugo, amore e polpette!
Ai miei fratellini Luna, Giammi e Chicco: siete il mio cuore.
GRAZIE

Table of Contents

List of Tables

List of Figures

Acronyms

AMR
Adaptive mesh refinement

BEM
Boundary element method

CFD
Computational fluid dynamics

DOF
Degree of freedom

FFT
Fast Fourier transform

FVM
Finite volume method

LES
Large Eddy Simulation

OWE
Offshore wind energy

RANS
Reynolds Averaged Navier Stokes

SPH
Smooth particle hydrodynamics

VOF

Volume of fluid

WEC

Wave energy converters

Chapter 1

Introduction

The worldwide goal of our generation is to leave our planet better than how we found it, and one of the best ways of doing that is by shifting to more sustainable ways to generate power.

The renewable sources based on solar and wind energy are already deployed. In particular the focus of this thesis will be the eolic generation: wind turbines are pretty common in windy areas where they often cause noise and visual pollution, but by locating these structure in the sea, those mentioned problems would be avoided, allowing to make the turbines bigger than the already gigantic onshore structures .

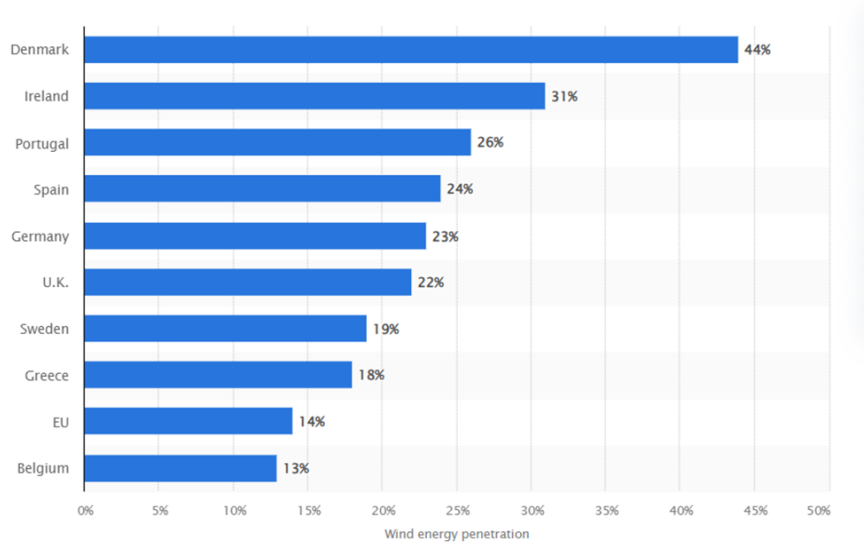

Figure 1.1: wind energy penetration in the electric grid in the EU as reported by Statista

As reported by the International Energy Agency, "*In 2022, of the total 900 GW of wind capacity installed, 93% was in onshore sites, with the remaining 7% in offshore wind farms. Onshore wind is a developed technology, present in 115 countries around the world, while offshore wind is at the early stage of expansion, with capacity present in just 20 countries. Offshore reach is expected to increase in the coming years as more countries are developing or planning to develop their first offshore wind farms. In 2022, 18% of total wind capacity growth of 74 GW was delivered by offshore technology*" [1].

Some countries in the EU are already using their wind resources to an optimal level, as reported in figure 1.1, 44% of Denmark's energy demand is satisfied by onshore and offshore turbines. The offshore wind park in Middelgrunden, just 3.5 km from Copenhagen, is a brilliant example of exploiting this resource to the fullest.

In the latest years the market is rapidly increasing, led by the huge investments of China. The global offshore wind market grew nearly 30% per year between 2010 and 2018. The article [1] also analyses the wind market possibilities, underlying that the actual status is still far from reaching its maximum potential, especially for the offshore wind parks, that could theoretically produce more than 420 000 TWh per year worldwide, this is more than 18 times global electricity demand today.

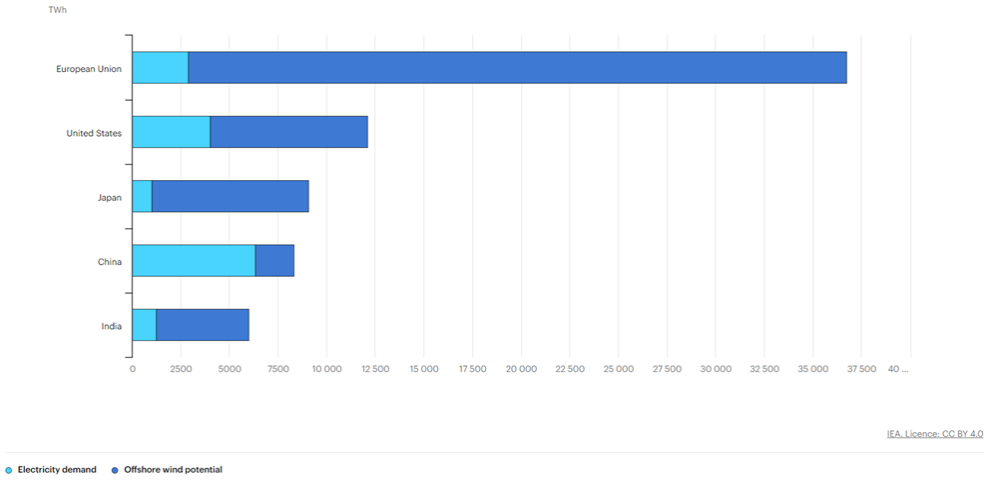

Figure 1.2: IEA, Offshore wind technical potential and electricity demand, 2018, IEA, Paris

The major advantages of OWE (offshore wind energy) plants over their onshore counterparts are lower wind shear, less turbulence, higher wind speed and availability of a larger continuous area. Water exhibits less surface roughness than land (especially deeper water), so the average wind speed is usually higher above open

water. Offshore wind turbines are also less obtrusive than turbines on land, as their apparent size and noise can be mitigated by distance, explaining why the biggest wind turbines are all situated offshore. To have a reference the giant Goldwind GWH252-16MW has a 252 m diameter and is the biggest in the world, producing up to 384.1 megawatt hours (MWh) in one day. The biggest onshore one is the EN-220/10MW with a diameter of 110 m , less than half of the former one. The turbine achievable power can be evaluated as: $P = \frac{1}{2}\rho V^3 S C_p$, thus having a bigger surface clearly increases the power available. As the reader could imagine, building a 200 m rotating structure is already complex on mainland and in open water things can only get harder. There are two possible ways to install those turbines: installing the main structure directly into the seabed, or making it float, harboured to the sea just to keep it in place and prevent it from travelling around the seven seas. This second solution seems to be more promising, because the floaters can be assembled in the harbour and then towed to the desired position. The downside to consider is the more complex structural stress of these type of turbines which will be better studied in the following chapter.

Chapter 2

Forces involved

2.1 Forces on the floating structures

In order to properly analyse all the loads on the structure, time domain models are required. Eq. 2.1 represents all the forces acting on the system, without specifying the way they interact. The reference is the paper [2], which refers to Wave Energy Converters (WEC), but the forces are the same for the structure of a floating wind turbine, with the precaution of considering the greater impact of wind, secondary in WECs.

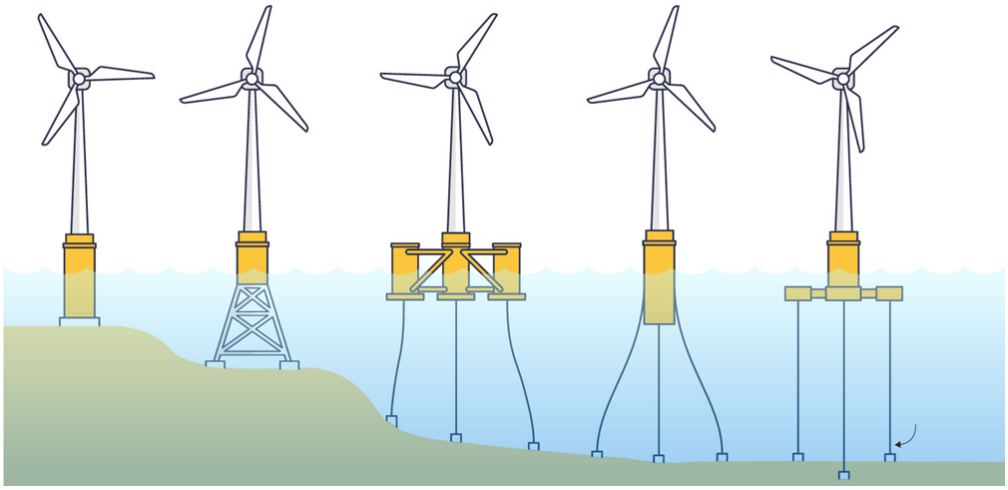

Figure 2.1: Possible configurations of offshore wind turbines. Sources: NREL, Aqua-RET

$$MX''(t) = f(F_g, F_{FK}(t), F_{\text{diff}}(t), F_{\text{rad}}(t), F_{\text{vis}}(t), F_{\text{PTO}}(t), F_{\text{moor}}(t), F_{\text{add}}(t)) \quad (2.1)$$

- F_g is the gravity force.
- F_{FK} is the Froude-Krylov force, the load introduced by the unsteady pressure field generated by undisturbed waves. It is generally divided into static and dynamic forces. The static part represents the relation between gravity and buoyancy forces in a static situation with a still ocean, while the dynamic part represents the force of the incident wave.
- F_{diff} is the diffraction force, refers to the bending or spreading of waves as they encounter an obstacle or aperture. In the context of floating structures diffraction occurs when waves encounter the structure and are dispersed or bent around it. This bending of waves around the structure can result in changes to the wave pattern and distribution of wave energy, impacting the forces acting on the structure.

  Diffracted and Froude-Krylov forces combined are the force caused by an incident wave on a steady body.

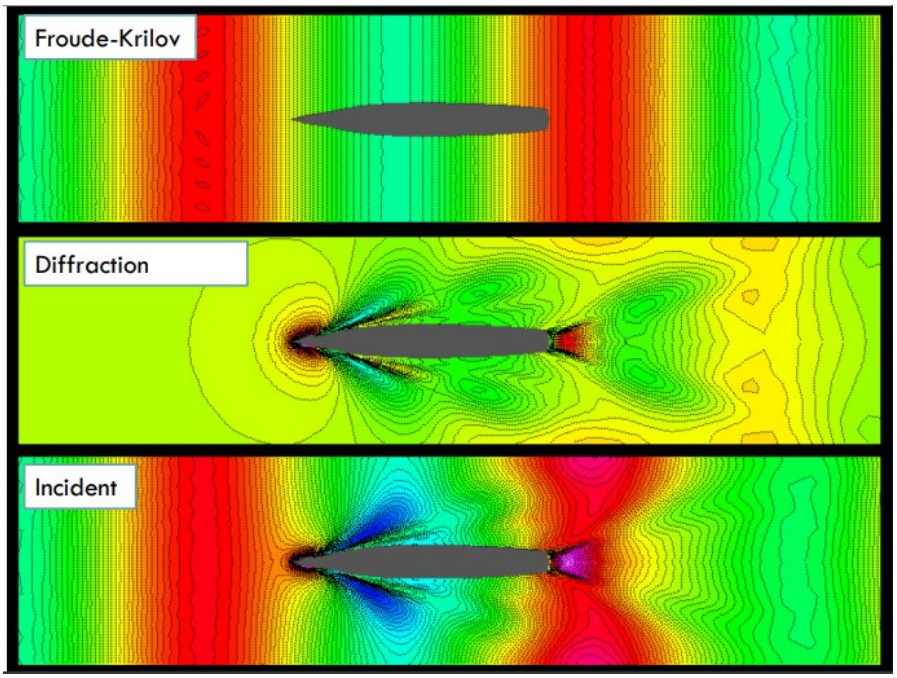

Figure 2.2: Visual representation of the pressure field of an incident wave on a steady body

- F_{rad} is the radiation force: when waves interact with a floating structure, they induce motions in the structure, causing it to move and experience forces. These forces arise due to the transfer of momentum from the waves to the structure. Radiation forces include both the inertia forces resulting from the acceleration of fluid particles around the structure and the added mass forces due to the volume of fluid displaced by the structure.

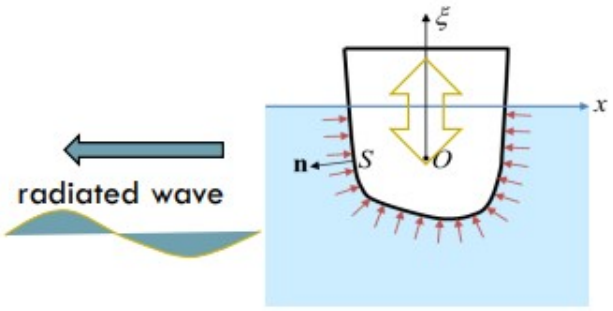

Figure 2.3: Radiated wave

To simplify the analysis, in the simulation for this thesis a certain motion is imposed on the floating body in steady water, causing radiated waves, in this way only the radiated forces will be considered.

In summary The FK forces are caused by the pressure field of the undisturbed waves, while radiation and diffraction consider the interaction with the submerged structure; diffraction deals with the bending or spreading of waves as they interact with a structure, affecting the distribution of wave energy, while radiation forces refer to the forces exerted on the structure by waves due to the transfer of momentum from the waves to the structure. These three phenomena are essential in the analysis and design of floating structures in wave environments.

- F_{vis}, the viscous force, is often neglected in the traditional offshore industry, in which hydrodynamic models have been mainly based on linear potential flow theory. Viscous losses are considered relevant for structures that are small compared to the wave amplitude. Since offshore structures are, in general, relatively large (offshore oil and gas platforms or ships), viscous losses are minor losses, except for localized effects, such as vortex shedding generation in sharp edges. Depending on the dimensions of the floating structure this effect could be relevant and is going to be analysed later in this thesis.

- F_{PTO} is the force acting on the structure due to the power take off system, depends on the energy generation system but is reasonably neglectable in Eolic turbines.

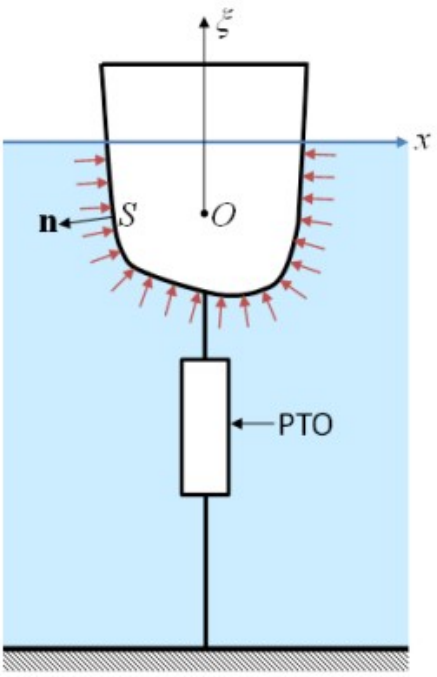

Figure 2.4: Scheme of a PTO system

- F_{moor} is the force due to the mooring lines, needed to keep the structure in its desired position. The forces can be considered as linear if the mooring is tight, but nonlinearities have to be taken into account for slacker structures [2].
- F_{add} is the force corresponding to any other additional force, such as drift, wind, tidal or other body-water interactions. The major effect is the wind that can't be ignored in wind turbines.

The safety of the floating structure and mooring system of floating wind turbines is crucial. It is necessary to investigate the motion responses (e.g. surge, sway, heave, roll, pitch and yaw) of the floating structure and mooring tension response.

Chapter 3

Fluid models and computational approaches

In the field of floating structures, the choice of physical model largely depends on the specific application. These models can generally be categorized into two main theories: potential flow and RANS-based models (Reynolds Averaged Navier-Stokes), each with its own advantages and limitations. Given the complexity of the problem, fully analytical solutions are impractical, requiring the use of various computational methods tailored to each physical model. This chapter provides a brief overview of the principal approaches, highlighting the contexts in which they are most effective.

3.1 Potential flow

The Potential flow model is valid for inviscid and irrotational flows, under these hypotheses exists a potential of velocity, which respects the Laplace equation $\nabla^2\phi = 0$, making the Green theorem applicable. The velocity of the flow is described as the gradient of the velocity potential, which can be decomposed into incident, diffracted, and radiated potentials.

Starting from the continuity equation:

$$\frac{D\rho}{Dt} + \rho\nabla \cdot \mathbf{V} = 0 \tag{3.1}$$

Known that for an incompressible flow:

$$\nabla \cdot \mathbf{V} = 0 \tag{3.2}$$

and putting that in the momentum equation,

$$\frac{d\mathbf{V}}{dt} + \mathbf{V} \cdot \nabla\mathbf{V} = -\frac{1}{\rho}\nabla p + \mu\nabla^2\mathbf{V} + \mathbf{f} \tag{3.3}$$

The potential flow considers the FK forces, the radiation and diffraction forces, underestimating the loads on the structure and ignoring the viscous forces, but has a lower computational cost compared to other methods. A CFD simulation based on the RANS, also considers the viscosity of the fluid, but the downside is the way higher computational cost.

A good compromise, which will be pursued in this thesis, is using the CFD simulation on particular cases: loading the structure at different frequencies and studying its damping; based on the results of these simulations, they will be used as corrections in the potential flow linearized model, keeping its low computational cost, but with an higher fidelity.

3.1.1 BEM

The computational translation of the Potential Flow theory is the BEM (Boundary Element Method), a numerical computational technique used for solving linear partial differential equations that have been formulated as integral equations. In the context of marine and offshore engineering, BEM is particularly well-suited for analyzing the linear interactions between waves and floating structures. It offers a good balance between accuracy and computational efficiency for small to moderate wave interactions. It is used in various softwares such as WAMIT, AQWA, NEMOH, HYDROSTAR, DIFFRAC and AQUADYN.

BEM transforms the problem into a boundary integral equation using Green's functions, or fundamental solutions of the Laplace equation, reducing the complexity of solving fluid flow problems by focusing only on the boundary of the domain. This reduction in dimensionality makes BEM highly efficient. The solution is then determined by discretizing the boundary of the domain (the surface of the floating structure and the free water surface) into small elements or panels.

This method is commonly used to model the hydrodynamic interactions in wave energy converters (WECs) and other offshore structures where the linear wave assumption holds.

BEMs struggle with highly nonlinear conditions such as large wave amplitudes or breaking waves. They also do not inherently include viscous effects, which may need to be added separately if significant.

3.2 RANS

In the Reynolds averaged Navier Stokes model, turbulence and viscosity are also considered for a Newtonian, incompressible Fluid. In a turbulent flow there is a continuous fluctuation of its variables, whose time average is zero, based on this hypothesis the velocity can be divided in two contributes. The equation is given

by:

$$u(x,t) = U(x) + u'(x,t) \tag{3.4}$$

Where u' is the perturbation and U is the average value. Under these hypotheses, the Reynolds Averaged Navier Stokes equations (reasonably neglecting the energy equation for low velocities) become:

$$\frac{dU_i}{dx_i} = 0 \tag{3.5}$$

$$\frac{\partial U_i}{\partial t} + U_j \frac{\partial U_i}{\partial x_j} + \overline{u'_j} \frac{\partial \overline{u'_i}}{\partial x_j} = \overline{f}_i - \frac{1}{\rho} \frac{\partial \overline{p}}{\partial x_i} + \mu \frac{\partial^2 \overline{u}_i}{\partial x_j \partial x_j} \tag{3.6}$$

Where f_i is a vector containing the external forces.
In Computational Fluid Dynamics, RANS are the most used for their simplicity, competing with LES and DNS, more precise but with way higher computational cost: what differs between this three approaches is how they consider turbulence. In ascending order of computational cost:

- LES (large eddy simulation) equations resolve the turbulence only for eddies above a certain filter dimension, while the smaller ones are handled introducing subgrid terms.

- DNS (Direct Numerical Simulation) resolve the NS equations for each particle, thus representing the most expensive option in terms of computational cost, growing with the third power of the Re number; this means it is applicable only to particular cases with a really low Reynolds, for example in the biomedic field.

3.2.1 CFD

CFD (computational fluid dynamics) involves solving the numerical solution Navier-Stokes equations to simulate the behavior of fluids. This method can handle complex, turbulent flows and can model the free surface using techniques like Volume of Fluid (VOF) or Level-Set methods. CFD provides detailed flow information, including the effects of turbulence and viscosity, making it suitable for scenarios where nonlinear effects and complex fluid interactions are important. It is widely used in simulating WECs, especially in cases where accurate modeling of the free surface and wave-body interaction is crucial. CFD is also beneficial in studying wave breaking, slamming, and other highly nonlinear phenomena. The limitations of these approach are that it is computationally expensive and time-consuming, particularly for three-dimensional simulations and when high resolution is required.

3.2.2 SPH

Another way of computing the NS equations is the Smooth-particles hydrodynamics. The SPH method is a purely Lagrangian meshless interpolation, that can approximate continuously field quantities and their derivatives by using discrete sample points, called smoothed particles. The fluid is represented by a collection of particles. Each particle carries properties such as mass, velocity, pressure, and position, and these properties move with the particles through space as the fluid evolves. The fundamental equations governing the fluid motion (RANS) are discretized and solved using the SPH formulation. The differential operators (such as gradient and divergence) are here replaced with interpolations over the particles using a smoothing kernel function.

It was originally developed for astrophysics [3], but has been applied to diverse applications, it is highly adaptable to complex and dynamic environments, such as breaking waves and highly nonlinear interactions, and can handle large deformations and fragmentation without remeshing, making it perfect for extreme event simulations (e.g., tsunamis, slamming). The disadvatage is that it is more computationally expensive than BEM and CFD, and less accurate for simple, linear problems. The method also suffers from pressure noise, which can be mitigated but often at the cost of increased computational effort.

To sum up, all the methods presented in this chapter have their specific domains of application, and the choice of it often depends on the balance between computational resources, required accuracy, and the nature of the wave-structure interaction problem being studied .

Chapter 4

Software introduction and simulation setup

4.1 Software introduction

The CFD software used is star-CCM+ (acronym of *Simulation of Turbulent flow in Arbitrary Regions - Computational Continuum Mechanics*), it allows to simulate the state or the evolution of a system, based on the RANS model.

The basic concept for space discretization is that the computational domain is divided into control volumes (or cells), which form the grid or mesh. Considered the complexity of this test case the mesh is unstructured, meaning that it is necessary to store the connectivity matrix of each cell. A structured mesh permits a faster computation but it's compatible only with really simple geometries

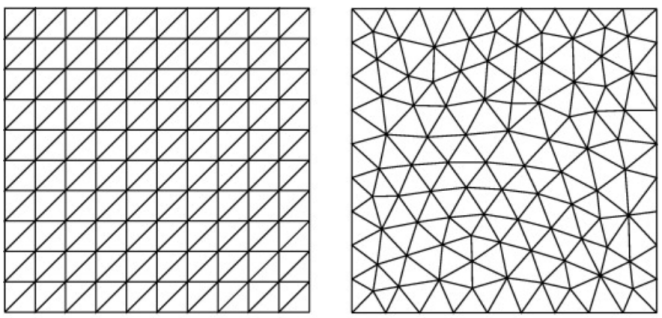

(a) Structured mesh (b) Unstructured mesh

Example of a structured triangular mesh and an unstructured triangular mesh in a unit box.

The values of the variables (such as velocity, pressure, and temperature) are stored at the center of each control volume. The FVM (Finite volume method) used by Star works by integrating the governing equations (in this case the RANS)

over each control volume, transforming them into algebraic equations.

$$\frac{d}{dt}\left(\int_V \mathbf{U}\, dV\right) = -\int_S \bar{\mathbf{F}} \cdot \bar{n}\, dS + \int_V q\, dV$$

Considering that in this case there are no sinks and sources, so the last integral can be deleted. Defining $\bar{\mathbf{U}} = \frac{\int_V U\, dV}{V}$ as the integral average of the variable U in the cell, the previous equation becomes:

$$V\frac{d\bar{\mathbf{U}}}{dt} = -\int_S \bar{\mathbf{F}} \cdot \bar{n}\, dS$$

In this way, known the fluxes, which are functions of the variables, the time derivatives are calculated, varying with the time integration method chosen. The flux method to apply deeply varies in function of the problem studied. The flux of quantities (like mass, momentum, or energy) across the control volume boundaries is calculated and then used in the next iteration to upload the values of the variables. In our simulations the goal is to study the structure dynamic response at various frequencies, this can be done generating waves and analysing the motion of the floating body, or imposing directly on the body the displacement and evaluating the radiated waves and forces; the second option is the one selected for this thesis.

4.2 Simulation setup

4.2.1 Geometry

The first step is importing or creating directly in STAR the needed geometry. The goal of a simulation is to represent in the most accurate way the experimental test conditions: for floating structure the testing facilities are huge tanks filled with water, with the possibility to create or damp waves on the borders.

In this section all the parts (physical and not) used in the simulation are defined: the body that could be a simple floating sphere or a complete wind turbine, the offset created from the body (later used to create a moving mesh) and the volumetric mesh refinements of the desired dimensions.

In geometry there is another subsection called *operations:* in this section it is possible to unite, subtract, intersect, extrude the geometries and so on. The first step is creating the offset from the moving body and then subtracting the same body from it to get the holed sphere where the mesh will be built.

Another fundamental part of 'operations' is the meshing: selecting the *regions* to be meshed, here the dimensions and the form of the cells are chosen. In this type of simulation there are two meshes: the tank mesh and the overset mesh.

4.2.2 Tank Mesh

It involves all the computational domain, so it is important to choose a good compromise between smaller cells that guarantee a more accurate solution and bigger ones that reduce the computational cost. The basic idea is to have smaller cells where the gradients are bigger, in these simulations this will be near the moving body, and slowly increasing the size of the cells going to the tank boundaries. This is achieved by adding volumetric meshes refinements with increasing mesh size.

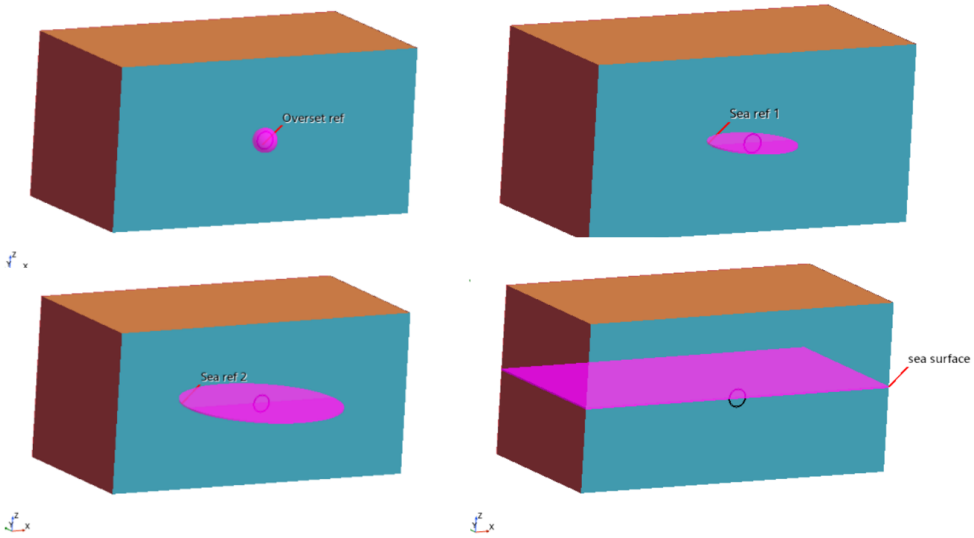

Figure 4.1: Volumetric refinements

4.2.3 Overset Mesh

The overset mesh is the closest region to the moving body, so it must be the most precise part of the Mesh. A polyhedral mesher is used instead of the trimmed used for the tank, the size of the cells is smaller and to have a good representation of the viscous effect of the body on the water a prism layer is added, its dimension will be coherent with the studied phenomenon.

4.2.4 Continua

In this part the physics model used in the simulation are selected, if needed it's possible to select different models to associate with different regions, this feature is not needed in this simulation so there will be only one model called Physics 1. In the picture 4.4 are shown the models selected, most of them are selected by default in Star so only a few of them will be briefly discussed.

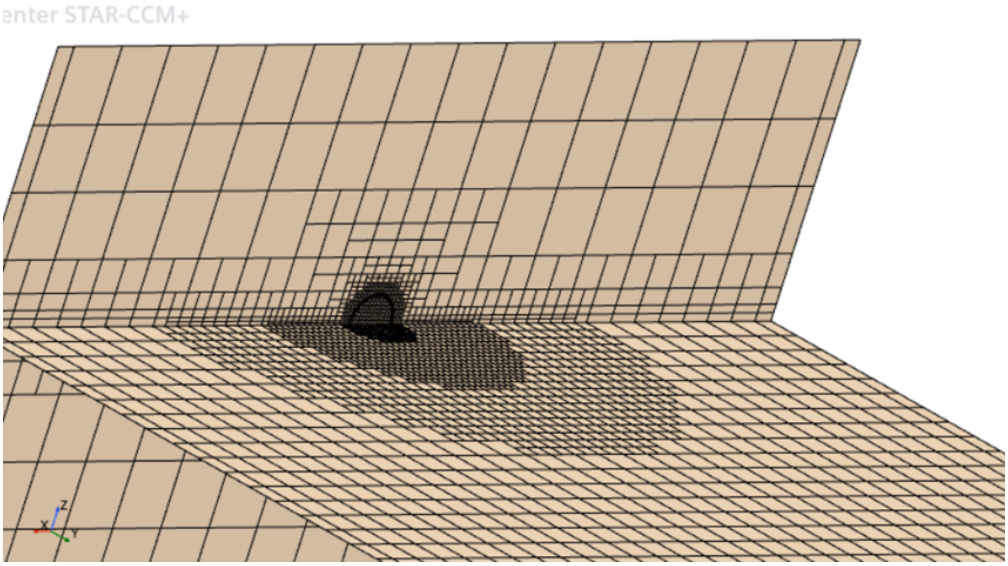

Figure 4.2: Tank mesh example, in the actual simulation the mesh will be way smaller and with more refinements.

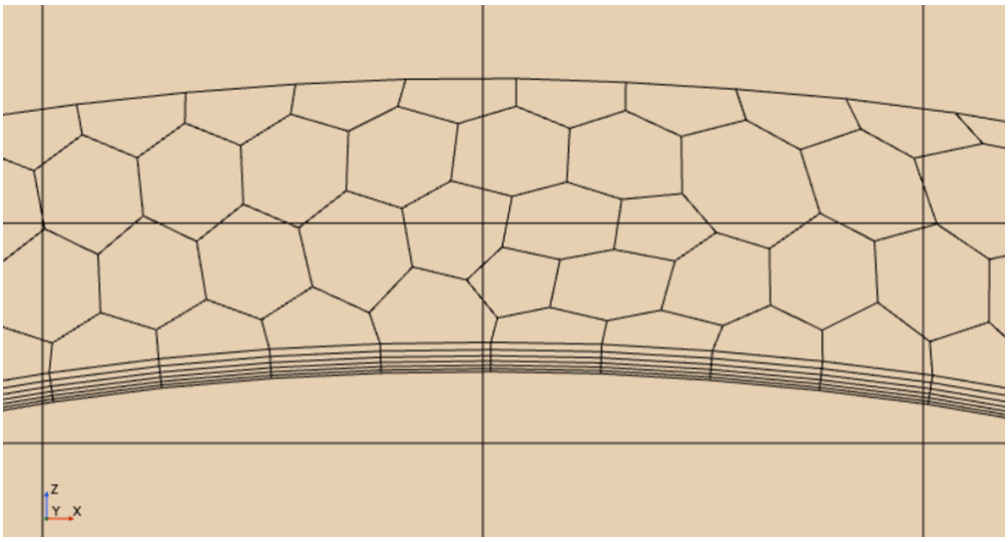

Figure 4.3: Detail of Boundary Layer

VOF

As mentioned in [2] of the main issue when modelling floating structures using CFD is the presence of a free-surface. Specific free-surface modelling techniques have been developed, which can be classified into two main categories: fitting methods (also known as tracking methods) [4] and capturing methods [5] . The tracking method

models the free surface as a sharp boundary, while the interface-capturing method includes water and air in the mesh, adopting either the volume of fluid (VOF) method [6] or the level-set formulation. The VOF is selected for this project. Every cell is identified by a VOF vector with two values between 0 and 1: [0 1] meaning it is just air and [1 0] only water, so a cell with half water and half air would be [0.5 0.5]. The phenomenon studied is time dependant so a 3D implicit, unsteady model is chosen. The accuracy of VOF simulations is sensitive to the mesh resolution. A finer mesh can more accurately capture the interface but increases computational cost. Adaptive mesh refinement (AMR) is enabled in this simulations, which refines the mesh only near the interface to optimize computational resources.

Turbulence Model: K-eps

The turbulence model used to close the RANS system is *K-eps*, one of the most common turbulence models used in CFD, which consists in adding two transport equations: one for K, the Kinetic energy of the fluctuations, and one for ε, the dissipation caused by the turbulence. For more information see [7] pag.122.

Other model selected

In the *continua* section the reference values are left as default, but the initial conditions need to be selected. In detail, the initial pressure field is the hydrostatic one for flat waves, and the velocity is that of the flat wave 1 model. In VOF waves it is initialized the height of the water surface at the beginning of the simulation.

4.2.5 Regions

In this section the desired parts are assigned to a region with the physical models selected in *Physics_1.* In our simulation the regions are the Tank and the Overset. Each part surface is here turned into a boundary.

Tank

The part assigned to this first region is the testing tank, creating a boundary for each part surface. The bottom surface z=L- is defined as a no-slip wall, as it is far enough from the water surface for being nearly irrelevant to the evolution of waves. A symmetry plane is defined for the plane y=0, as the simulation is symmetrical: in this way there will be half the cells of the complete simulation, obtaining the results in the other half just by mirroring them, saving a lot of computational cost.

The upper surface of the tanks is set as a pressure outlet, with a constant volume fraction of [0 1] (only air); the other specification needed is the pressure value,

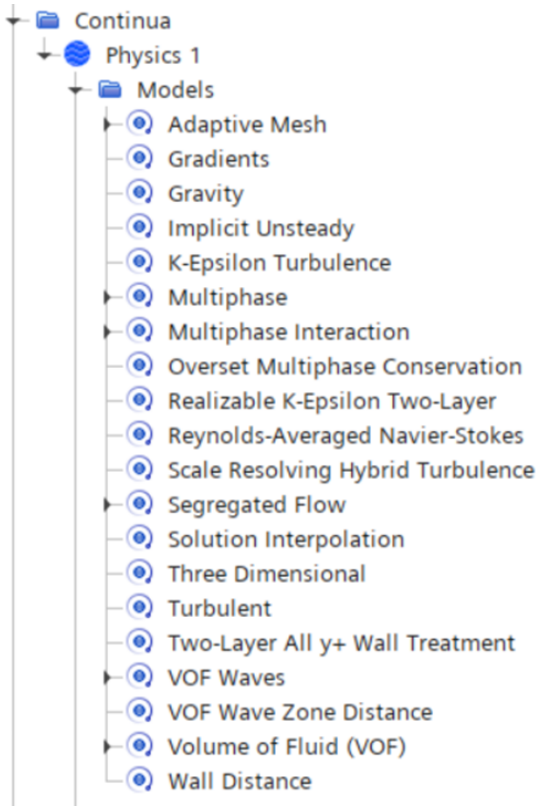

Figure 4.4: Section Continua

selected as 'Hydrostatic Pressure of Heavy Fluid of Flat VOF Wave 1', in this way it will vary coherently with the waves evolving.

The remaining surrounding surfaces of the tank (x=L+, L- and y=L) are all velocity inlets. The VOF selected is composite (both air and water). In the section Physics values the velocity model is that of the flat wave, adding a damping effect near the boundary from a selected length: that corresponds to viscous dampers such as grids in the testing facility, needed to avoid the reflection of waves hitting on the walls of the tank, because the goal is to reproduce the behaviour in the open sea.

Overset

In the Overset region there are three boundaries: the external surface of the overset, with type 'Overset Mesh', the symmetry surface and the surface of the body, with type 'wall', condition no-slip.

It is necessary to create an interface between the two regions, this volume-type interface provides coupling of solutions on the domains using automatically

generated sets of acceptor cells on one mesh and donor cells on the other mesh. Variable values at donor cells express variable values at acceptor cells through interpolation.

4.2.6 Automations

In the subsection 'Parameters' it is possible to make the simulation easier to modify, inserting here the various parameters used in the whole code, such as Base size of the Mesh, reference height of the flat waves, time step used and so on. Remaining under automations, another useful subsection is 'Field Functions', there is a huge number of functions present by default, with the possibility of adding new ones such as the Velocity of the body.

4.2.7 DFBI and Motion

The first step is creating a motion in the tools section: by default, the stationary motions is already there so it is necessary to create a new one of type 'DFBI Rotation and Translation', which needs to be selected in the motion specification of the Overset region. In the DFBI (Dynamic fluid-body interaction) section the process is DFBI > 6-DOF Bodies node and select New Body > 3D > Continuum Body, which creates a body called 'Body 1'. After renaming the body, the surfaces of the overset are selected. In this section all the Inertial data of the body are inserted: Mass, center of Mass and moments of Inertia. In the External Forces 'Fluid force and Moment' and Gravity Force are enabled.

The DOFs of the motion are Z translation (heave), X rotation (surge), Y rotation (pitch).

4.2.8 Stopping Criterias and Solver

An implicit method is needed to avoid excessive limitations on the time step: an explicit method is faster and more efficient but would require a way smaller time step for stability reasons, so it is only used in simulations where the time step is already really small, such as for resolving smaller scales of turbulence in the DNS simulations. In this case the RANS are used for modelling turbulence, so the 'implicit unsteady' solver is selected, with a second order temporal discretization. The stopping criteria are the inner iterations for each time-step and the physical time to simulate. Both will be discussed in the next chapter, because there's an important trade-off between quality of the results (which increase with both) and the computational cost which is basically directly proportional to them.

Time-step

The maximum time step value is selected so that, for any time step, the overset mesh moves by a distance smaller than half the height of the smallest cell in the boundary layer of the Tank region. A finer mesh would require an even smaller time step. In this example 4.5, considering a maximum velocity of 1 m/s, the time step must be less than 0.62 seconds. The final mesh used will be way smaller than the one in the picture, so the time step is parametrized in function of the dimension of the Mesh. It is important to consider that the cells near the free surface will be smaller than expected due to the AMR so it's important to choose a conservative value for dt.

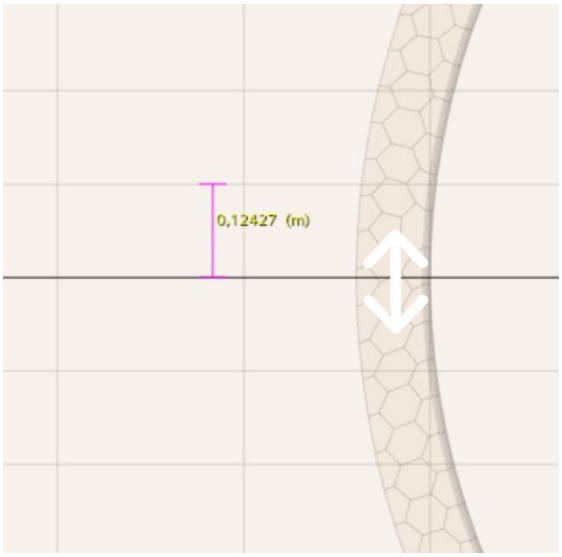

Figure 4.5: Mesh detail close to the sea surface

4.2.9 Reports, monitor and plots

A report presents a computed summary of the current simulation or CPU data. A node represents each report in the simulation tree, each with its own pop-up menu. Report properties, however, vary by report type.

The report summaries are useful for post-processing, and enable reporting values such as drag, lift, torque, or mass flows. They are also useful for computing diagnostic quantities such as minimum cell volume or average wall y+, in this example the monitor requested are Fz(t) and the displacement of the Center of mass with respect to the origin, to follow this displacement another system of coordinates called 'managed' is created in the tools section: the origin of this system *o'* moves together with the center of gravity *Cg* of the moving body, measuring the distance

from the o' and o (origin of the laboratory's fixed system) the evolution of z(t) is obtained and plotted. Another useful plot is the height of the water free surface at a certain reference point: this plot is obtained plotting the intersection between the isosurface VOF=0.5 (cells with half water and half air) and the plane x=0; this type of plot can be confronted with the movement of a buoy in a fixed position x,y in the testing facility to validate the results. The monitor saves and plots the report data. Here are some examples plotted for a heaving sphere subjected to a harmonic velocity with an amplitude of 0.1 m/s, excited at various frequencies. The following plots are for explanatory purposes only, as they were obtained using a simulation that is too coarse, which explains the oscillation of certain variables, such as the z-position 4.6.

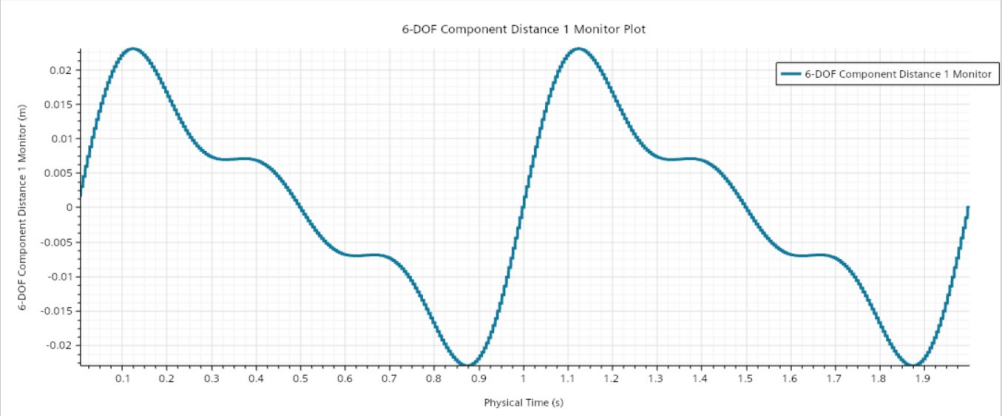

Figure 4.6: Z position of the heaving sphere

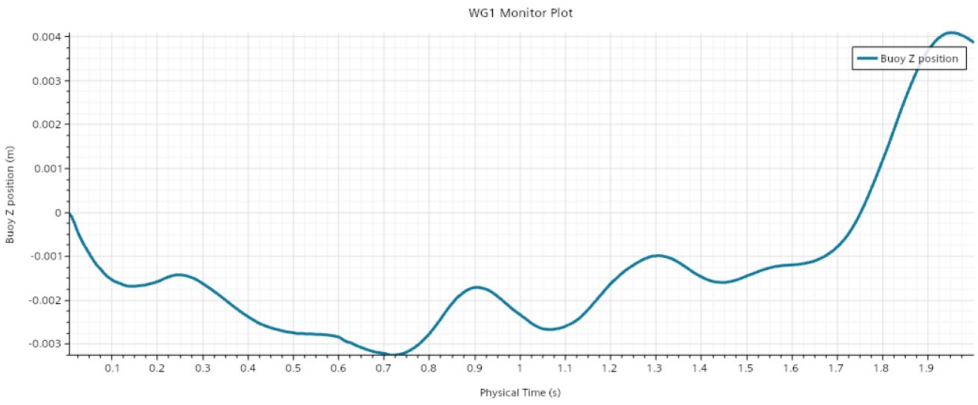

Figure 4.7: Buoy z position, located at 1 m from the sphere

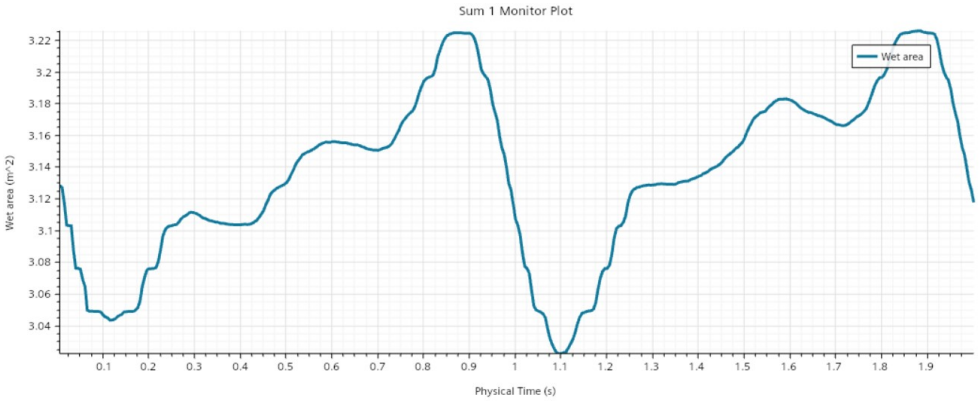

Figure 4.8: Wet surface of the Heaving sphere

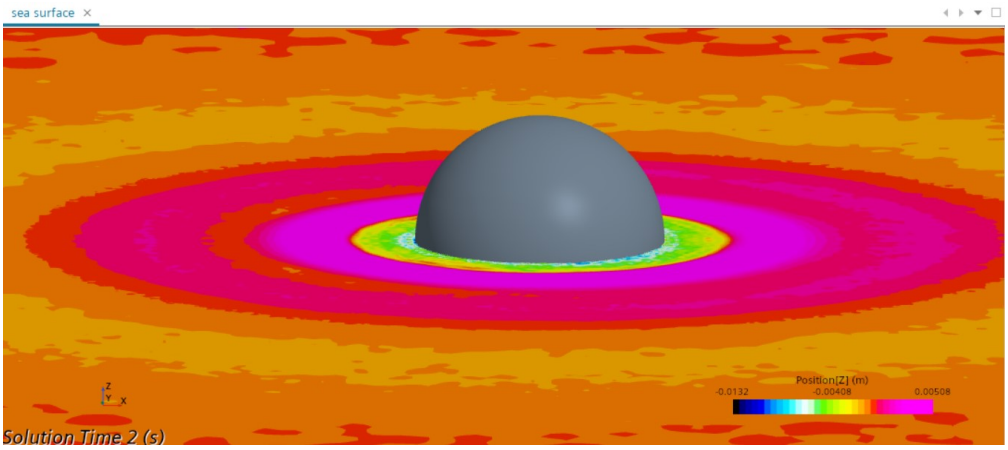

Figure 4.9: Sea surface scene at 2 s with heaving sphere

Chapter 5

Heaving sphere

The first comparison between the two methods is conducted on a simple system: a sphere with a radius of 1 m and a mass of 1000 kg, using the simulation setup shown in the previous chapter. NEMOH starts from the hypothesis of potential flow (inviscid and irrotational). With CFD, turbulence (modeled using a RANS model) and viscosity are also taken into account.

5.1 System model

The floating sphere system can be approximated by a mass-spring-damper system, corrected by considering the effect of the added mass $A(\omega)$, the inertia added to a system because an accelerating or decelerating body must move (or deflect) some volume of surrounding fluid as it moves through it. $A(\omega)$ is a function of frequency, and is often comparable to the real mass of the body, ignoring it could lead to relevant errors in the calculation. The following equations are obtained starting from the Cummins' relations [8].

$$(m + A)\ddot{\xi} + B\dot{\xi} + K\xi = \sum_{i=1}^{N} f_{\text{ext},i} \tag{5.1}$$

Each coefficient is a 6x6 Matrix, the DOFs are the translations on the three axis:

- X, surge
- Y, Sway
- Z, heave

and the corresponding rotations:

- RX, Roll

- RY, Pitch
- RZ, Yaw

Considering only the heave DOF, the motion equation for the z axis becomes:

$$(m + A(\omega))\ddot{x} + c\dot{x} + kx = F_{\text{hydro}}(t)$$

where m is the mass of the object, A is the third element on the diagonal of the 6x6 A matrix, c is the unknown term and k is the stiffness of the system, corresponding to the ratio between the variation of the hydrostatic force with respect to the displacement:

$$K = \frac{dF_{st}}{d\xi} = \frac{\rho \cdot g \cdot dV}{d\xi} = \frac{g \cdot \rho \cdot A_{wp} \cdot d\xi}{d\xi} = g \cdot \rho \cdot A_{wp} \tag{5.2}$$

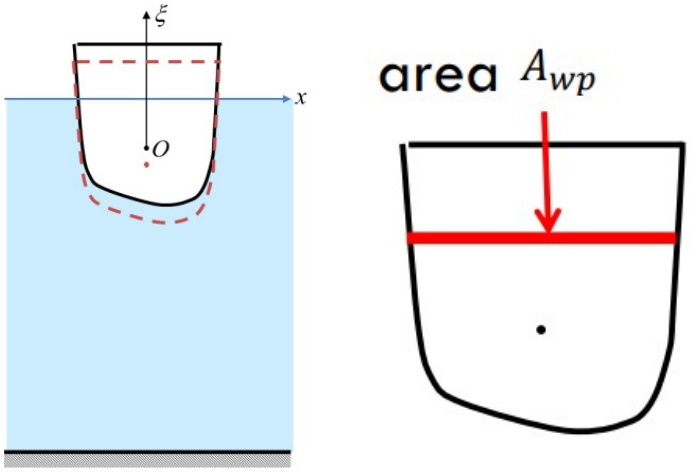

Transitioning to the frequency domain and solving with respect to velocity. The equation becomes:

$$i\omega(m + A(\omega))\dot{X} + c\dot{X} + \frac{k\dot{X}}{i\omega} = F_{\text{fft}}$$

Where F_{fft} is the fast Fourier transform of the hydrodynamic force exported from STAR, and $\dot{X}$ is the FFT of the velocity. The only unknown is the damping value $c(\omega)$, obtained as:

$$c(\omega) = \Re\left(\frac{F_{\text{fft}}}{\dot{X}} - (m + A(\omega))i\omega - \frac{k}{i\omega}\right)$$

Considering that the second and third term are only imaginary, the equation can be simplified as:

$$c(\omega) = \Re\left(\frac{F_{\text{fft}}}{\dot{X}}\right)$$

5.2 Software implementation

The idea is to impose a sinusoidal motion and extracting the Force report from STAR-CCM+ to obtain the damping. The only DOF considered in this case is the translation in the z direction (Heave), the most complex case would be considering all the 6 DOFs.

Imposed motion on the heaving sphere in these simulations:

$$V_z(t) = A \sum \sin(\omega_i t)$$

Imposing $\dot{x}$ and deriving F_{hydro} from STAR, transitioning to the frequency domain by performing the FFT, and solving with respect to velocity. The first optimistic attempt was to combine more frequencies in group of 6 for simulation, ranging from 1 to 85 Hz with $A = 0.1\,\text{m/s}$ and calculating the damping coefficient 'c' at those frequencies

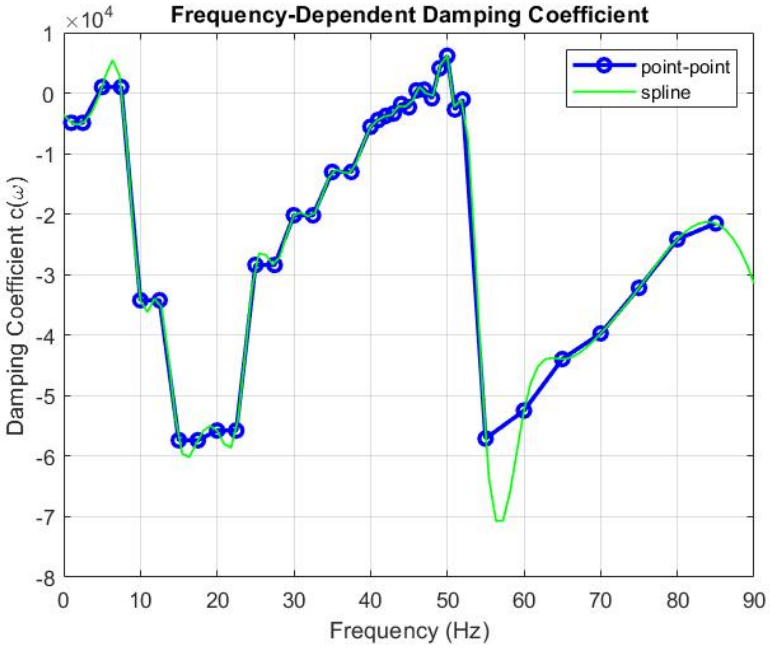

Figure 5.1: "Damping" obtained combining various frequency in the same simulation

Theoretically, CFD is a higher fidelity model compared to BEM, but it is necessary to consider the very coarse mesh used for simulations and the sensitivity of frequency analysis to the sampling method. The results shown in 5.1 are clearly unphysical, a negative damping means that that the system is unstable, there are various reason for these results:

- These simulation have been run with a mesh too big to reach convergence as shown by the plot of the residuals

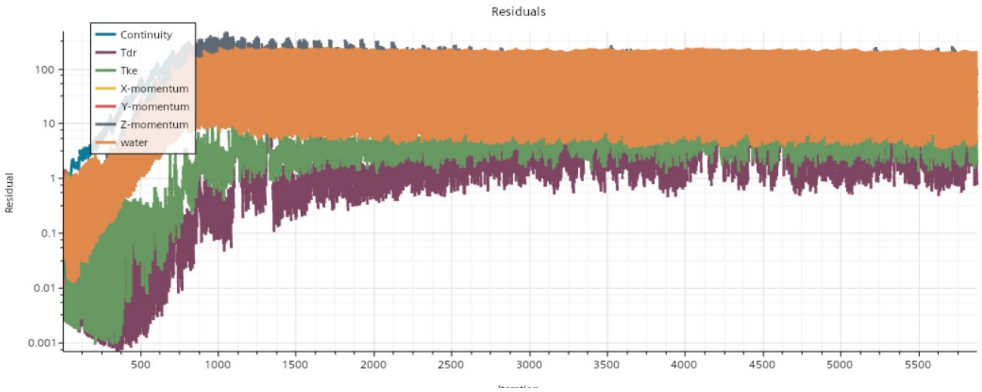

Figure 5.2: Residuals with base size of 500

- Trying to simulate such high frequency excitations demands an higher sampling frequency, needless to mention that in the context of waves reaching 1 Hz of frequency is already enough. The sampling was performed at approximately 106 Hz, using the timestep imposed to respect the condition explained in section 4.6, resulting in a dt= 0.009375 s.

- Combining too many frequencies in one simulation ruin the results, especially with a low frequency resolution as the one obtained in the previous simulations.

The following simulations are therefore run with a single frequency imposed motion, combining the results of each one during the post-processing phase to obtain a plot of the damping in function of the frequency.

$$V_z(t) = A\sin(\omega_i t)$$

$A = 0.5\,\mathrm{m/s}$, and ω_i corresponding to $f = [0.125; 0.25; 0.5; 0.75; 1]\,\mathrm{Hz}$. To have a proper time representation, at least one clean period is simulated for each frequency avoiding the transitory at the start of the simulation and respecting the 'golden rules of sampling' :

Sampling a periodic function to build its Fast Fourier Transform (FFT) involves adhering to several fundamental principles to ensure accurate representation and analysis. These principles are primarily guided by the Nyquist-Shannon sampling theorem and other considerations related to discrete signal processing.

Here are the rules used to post process the simulation results:

- To avoid aliasing, which is the misinterpretation of high-frequency signals as lower frequencies, the sampling rate is always at least twice the highest

Frequency present in the signal, $f_{\max}$. This is known as the Nyquist rate: $f_s \geq 2f_{\max}$. If $f_s < 2f_{\max}$, aliasing will occur, distorting the frequency components; anyway the time-step is imposed by the CFL condition explained in chapter 4, so the sampling frequency used for these simulations is at least 200 Hz, way higher than the Nyquist rate.

- The total sampling time covers an integer number of periods of the periodic function. This avoids discontinuities at the boundaries of the sampling window, which can introduce spectral leakage. The number of samples is chosen such that the sampling interval (the total time span of the samples) is an integer multiple of the period of the function.

- The frequency resolution of the FFT is determined by the total sampling time. Achieving higher resolution requires a longer sampling duration, as the frequency bin width is given by $\Delta f = \frac{1}{TimeSimulated}$. This creates a trade-off between frequency resolution and computational cost.

The first noticeable result shown in 5.4 and 5.3 in all simulations is that viscous forces are 3 orders of magnitude smaller than pressure forces, which are thus potentially negligible. However, pressure forces differ between the two models used by NEMOH and STAR, leading to different results in each case.

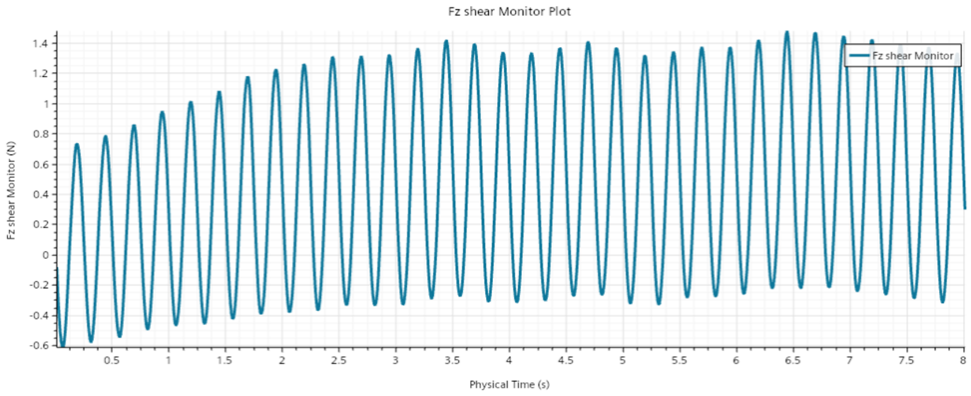

Figure 5.3: Shear Force for a 4Hz imposed motion

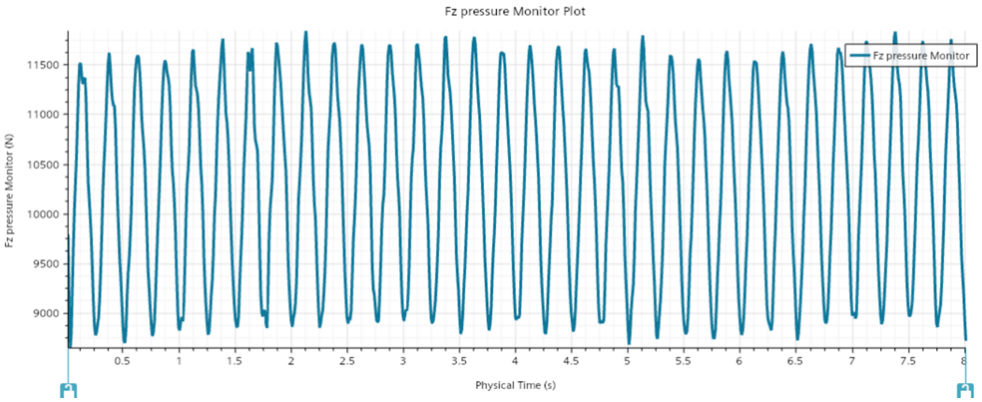

Figure 5.4: Pressure Force for a 4 Hz imposed motion

5.3 Comparison between the two models

As mentioned earlier, NEMOH is based on a lower fidelity method, relying on potential flow theory. The advantage of this approach is its significantly lower computational cost compared to the higher fidelity RANS model. In this section, the two methods are compared.

Here 5.5 the damping coefficient obtained from the BEM model for the z-direction of the sphere is plotted.

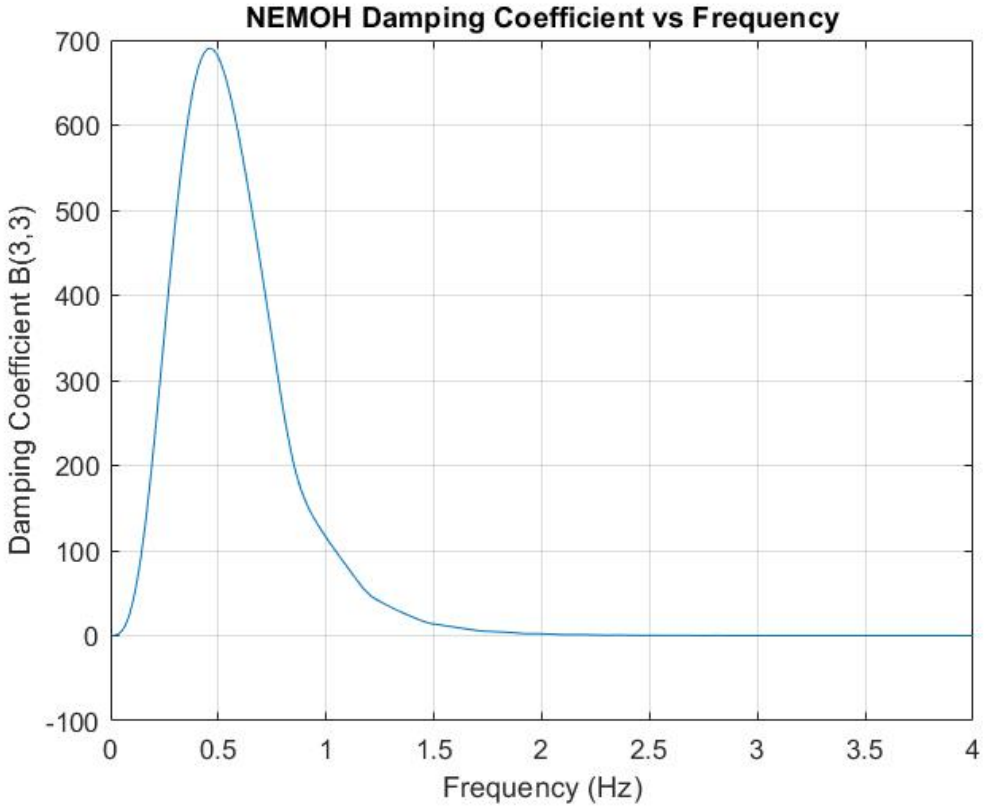

Figure 5.5: NEMOH damping from 0 to 4 Hz

The sphere no longer radiates for frequencies greater than 1.5 Hz, so the comparison between the two models is done between 0 and 1 Hz.

Linear wave theory

Considering the geometry of the simulated system, it is possible to verify if the system is within the linear region using the graph in 5.6.

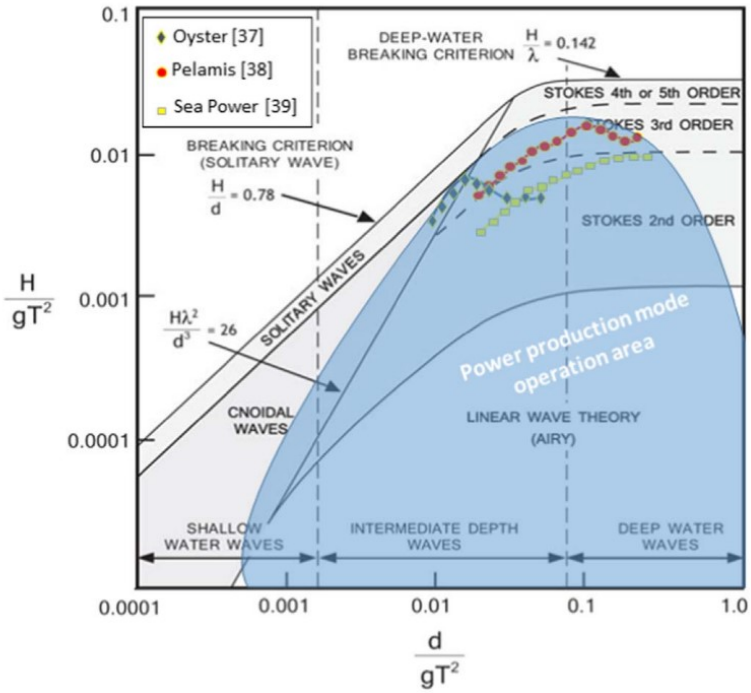

Figure 5.6: Area of validity of the linear wave theory [2]

Where T is the period, H is the height of waves, d the depth of water and g the gravitational constant. For the following simulations $\frac{H}{gT^2} < 10^{-2}$ and $\frac{d}{gT^2} \sim 0.5$, thus the linear field assumption are respected.

To verify the validity of the linear wave theory, a simulation with f=0.5 Hz is repeated with different values of 'A', the amplitude of the imposed velocity, ranging from 0.2 to 1.5 m/s.
In all the following simulations, the average force is 9.81 kN, corresponding to the weight of the floating body; this value is subtracted from the plot to better highlight the harmonic oscillations generated by the imposed motion.

- A=1.5 m/s

  The first simulation was run for an amplitude of A=1.5 m/s, resulting in a maximum displacement of 47.7 cm. The BODE plot 5.7 clearly shows that the only excited frequency is 0.5 Hz, as expected.

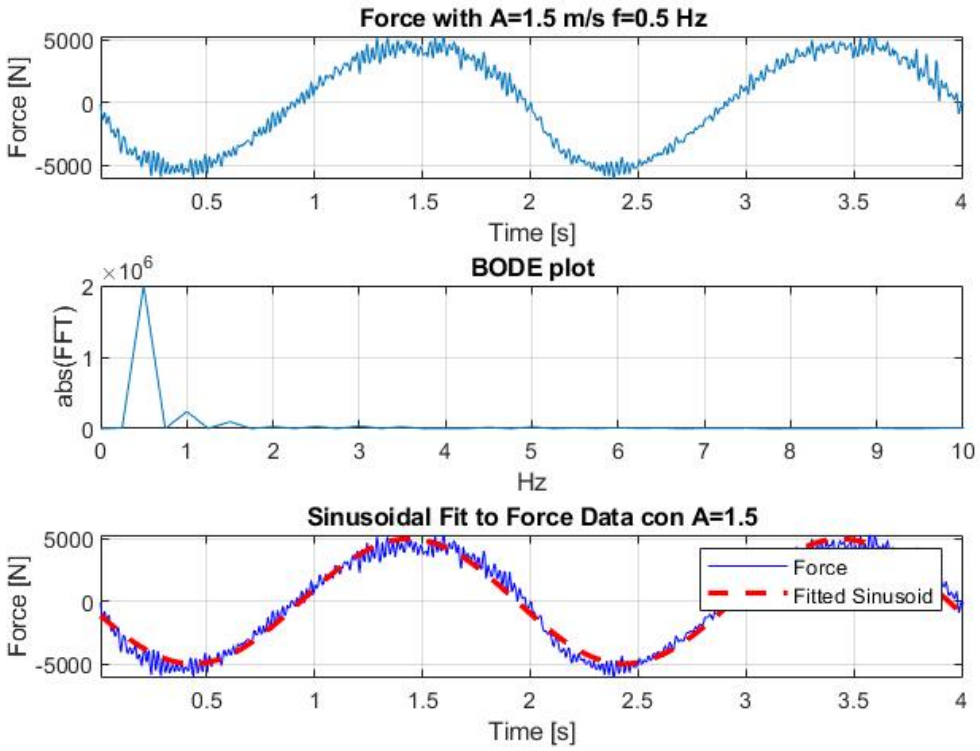

Figure 5.7: Plots for A=1.5 m/s f=0.5 Hz

The radiated waves have an amplitude of 16 cm, as they are proportional to the motion of the body. The phase shift between the displacement (ore the velocity) and the force is a useful tool to obtain the damping: if the phase is the same, as is the damping at various amplitudes. For this case ϕ=1.798 rad = 103.02°.

To ensure that the noise does not ruin the result, the phase is then calculated for the fitted sinusoid (red dotted curve in red5.7), yielding the same result.

- A=0.5 m/s

  The same procedure is repeated for A=0.5 m/s, resulting in a displacement of 15.9 cm that radiates waves of 5 cm.

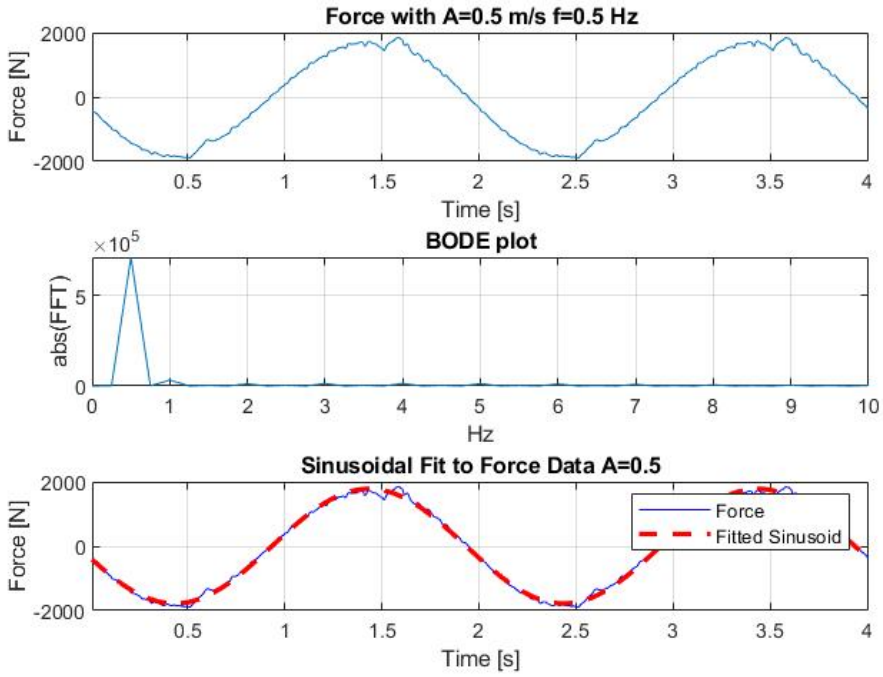

The phase is really similar to the previous case, obtaining now ϕ=1.807 rad = 103.5°, both for the actual force and its fitting. From here on, the fitted curve will not be plotted as it does not provide additional information.

- A=0.25 m/s

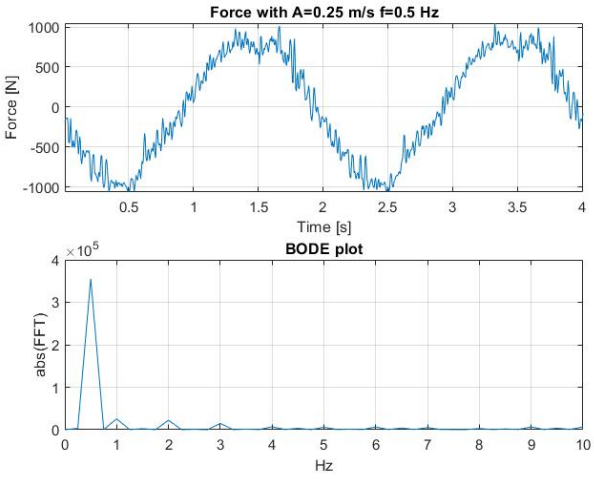

- A=0.2 m/s

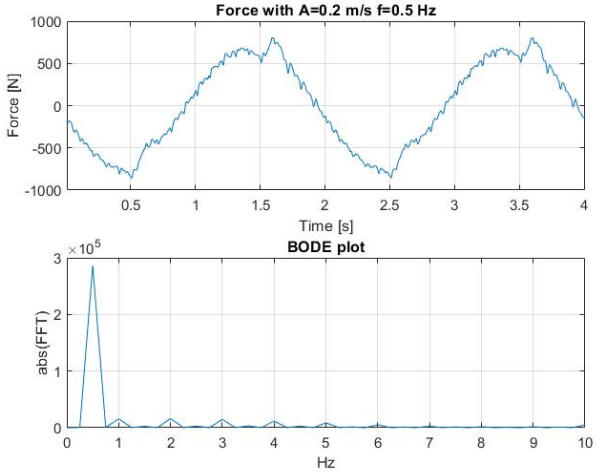

The following table summarize the results of this section:

A **[m/s]**	A_z **[m]**	$H_{\mathbf{wave}}$ **[cm]**	ϕ [°]
1.5	47.7	16	1.798
0.5	15.9	5	1.807
0.25	6.37	3.3	1.804
0.2	7.96	3	1.812

Table 5.1: various amplitude for f=0.5 Hz

Simulations with A=0.5 m/s with various frequencies

Having shown that the damping does not depend on the amplitude of the imposed motion in the previous section, its behavior across different frequencies is studied. The easiest amplitude to analyze is A=0.5 m/s, as it strikes a balance: the radiated waves are not too small (which would require a finer mesh and result in longer computational times) nor too large (which could cause issues with damping at the boundaries of the computational domain).
The chosen frequencies to accurately represent the frequency domain behavior of 'c' are 0.125, 0.25, 0.5, 0.75, and 1 Hz.

The lower frequencies, up to 0.5 Hz, require longer simulated physical times to capture several periods, but they are easier to identify, and the resulting plots are nearly perfect sinusoids.

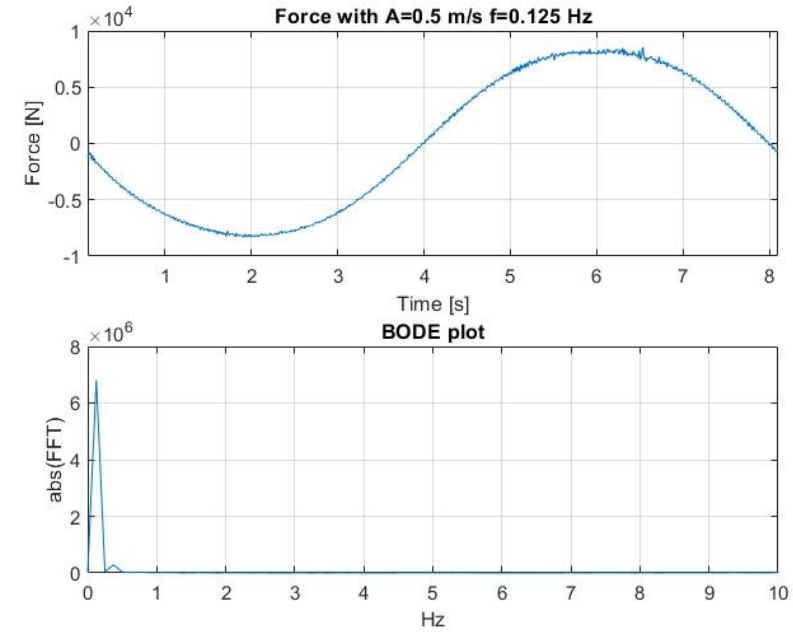

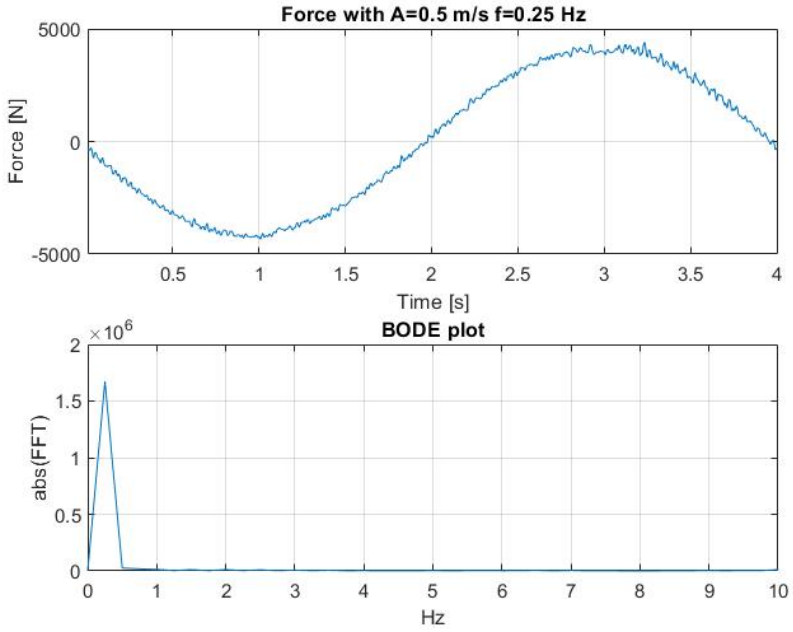

For 0.75 Hz and 1 Hz, the resulting forces are smaller, and the noise becomes increasingly significant, making it challenging to plot the results accurately.

The force at 1 Hz behaves unusually. Besides the noise, there is another excitation

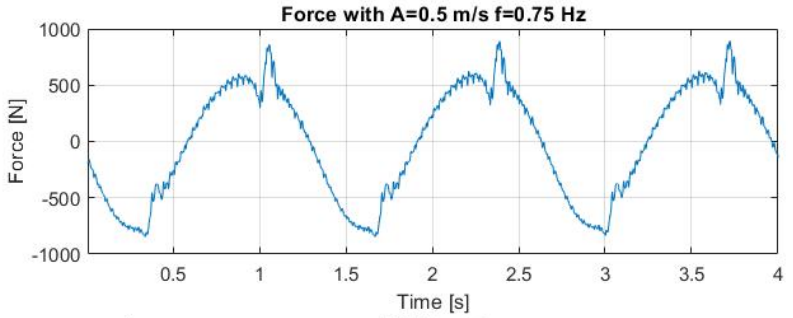

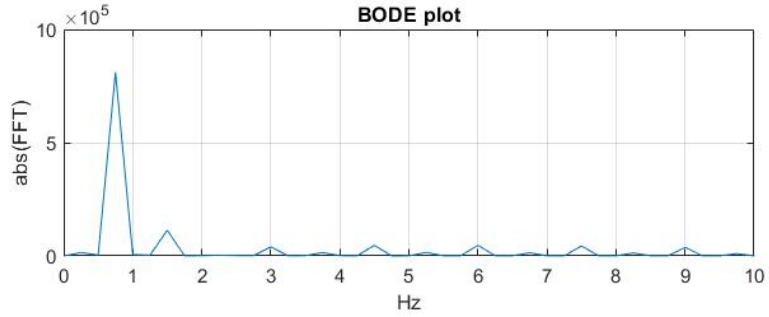

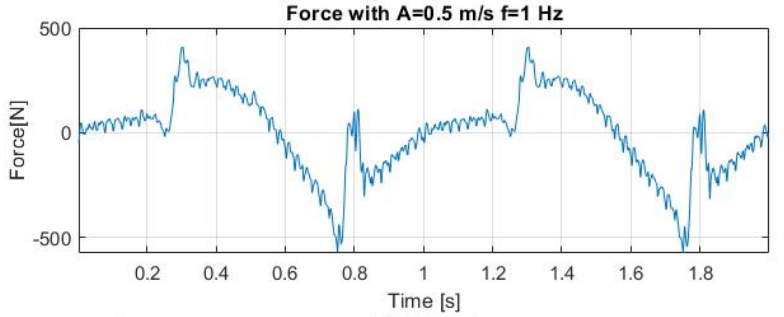

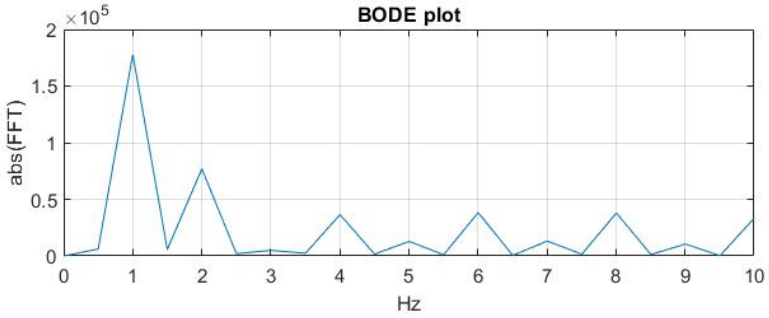

at 2 Hz and its multiples. This could be due to two reasons:

- Such a high frequency is difficult to capture and would require a finer mesh. However, repeating the simulation with the same mesh at 2 and 3 Hz produces

a better harmonic response, so this possibility can be excluded.

- Looking at the damping plot 5.8 ,there is a spike at 0.5 Hz. The system dissipates the maximum energy at this frequency, suggesting that it could be a natural mode of vibration. When the system parameters, such as stiffness or damping, are modulated at a frequency close to twice the natural frequency, parametric resonance (for more info [9]) can occur. This can cause energy to transfer from the primary oscillation to higher harmonic modes, leading to the spikes at 2 Hz and its multiples in the BODE plot.

Final Comparison

Combining the damping calculated for each of the previous simulations, the plot is compared to the one obtained using NEMOH. The behaviour is really similar, but the damping obtained through CFD is slightly larger, see 5.2.

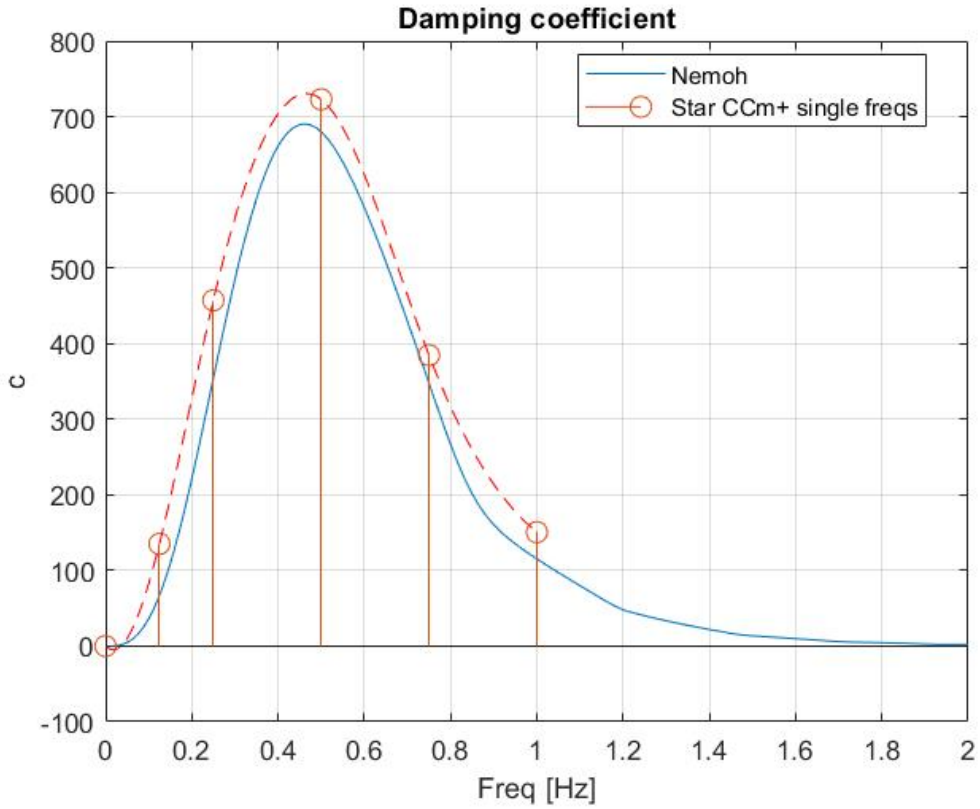

Figure 5.8: Damping comparison between the two models

Frequency [Hz]	**Nemoh Damping**	**Star Damping**
0.125	60.063	135.25
0.25	354.35	457.17
0.5	679.76	722.89
0.75	347.48	384.66
1	115.24	150.64

Table 5.2: Comparison of Nemoh and Star Damping across different frequencies

Chapter 6

Convergence analysis

Before considering the results of this type of simulation as correct, it is essential to validate them. The first step is to examine the residuals and ensure they are below a reasonable limit. For normalized residuals, they should be smaller than ten, and ideally less than one.

Iteration	Continuity	X-momentum	Y-momentum	Z-momentum	Tke	Tdr	water
3991	1.385761e-01	9.228320e-02	5.955596e-02	2.662865e-02	3.886477e-02	2.887138e-02	1.649849e+00
Reversed flow on 17957 faces on Tank: Tank.top 							
3992	1.541180e-01	1.942615e-02	1.331546e-02	9.273419e-03	7.788185e-03	5.810883e-03	2.208985e-01
Reversed flow on 17956 faces on Tank: Tank.top 							
3993	1.449682e-01	6.885886e-03	6.191821e-03	6.133594e-03	1.560599e-03	1.169701e-03	3.878125e-02
Reversed flow on 17956 faces on Tank: Tank.top 							
3994	1.374556e-01	5.199927e-03	5.082696e-03	5.032943e-03	3.128031e-04	2.375884e-04	1.266855e-02
Reversed flow on 17956 faces on Tank: Tank.top 							
3995	1.334394e-01	4.692260e-03	4.604722e-03	4.448835e-03	6.274197e-05	5.071729e-05	7.596755e-03

Figure 6.1: Residuals screen for A=0.5 m/s f=0.5 Hz

The second step in validating numerical simulations is to ensure they all converge to the same values when the physical phenomenon remains consistent. In this context, repeating the simulation with slightly different mesh sizes and confirming they converge to the same results is a good approach. The same excitation was applied to the sphere with the same mesh setup, changing only the base size, which ranged from 800 to 100.

The mesh with a base size of 800 was so coarse that the simulation crashed due to conflicts between donor and acceptor cells. The other simulations were run with an imposed velocity of:

$$V_z = 0.5\left(\cos(0.5\pi t) + \cos(\pi t) + \cos(1.5\pi t)\right)$$

This corresponds to frequencies of 0.25, 0.5, and 0.75 Hz. As the base size was reduced, the noise became progressively less significant, converging to the yellow curve (with a base size of 100) 6.2.

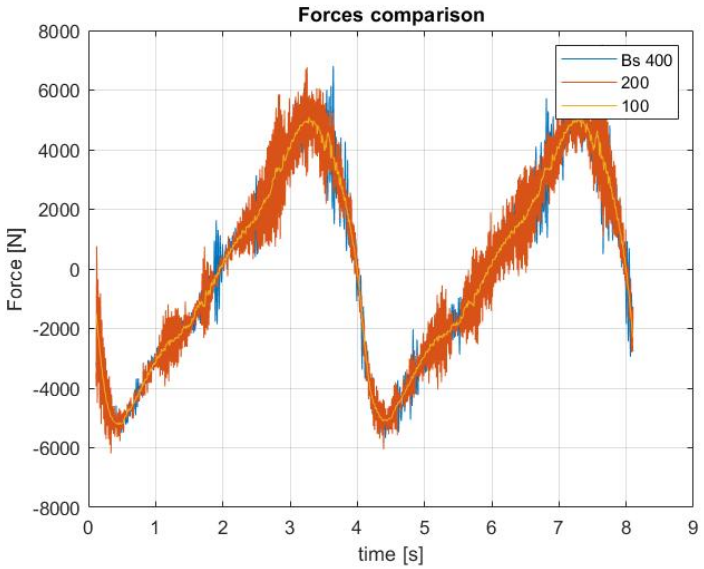

Figure 6.2: Force plot for 0.25, 0.5 and 0.75 Hz combined

To have a more complete damping behaviour, the simulation with a b.s.=100 was repeated reducing the dimension of the cells in the sea surface refinement and in the boundary layer, adding two cosines with the same amplitude at 0.25 and 1 Hz, resulting in the force plot 6.3.

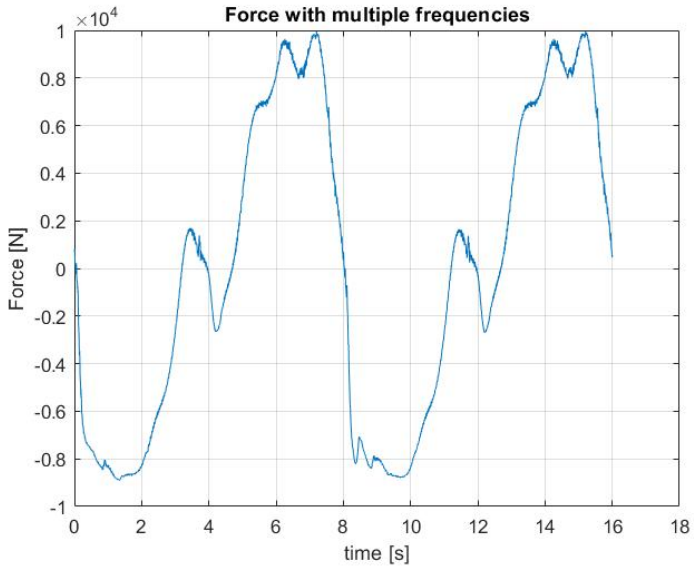

Figure 6.3: Force plot for 0.125, 0.25, 0.5, 0.75 and 1 Hz combined

Considering the difficulties to represent the 1 Hz frequency, as explained in the previous chapter, the 1 Hz damping value is not considered valid, plotting the results of all the previous simulations in 6.4, it is shown that the Star damping is very close to the BEM prediction.

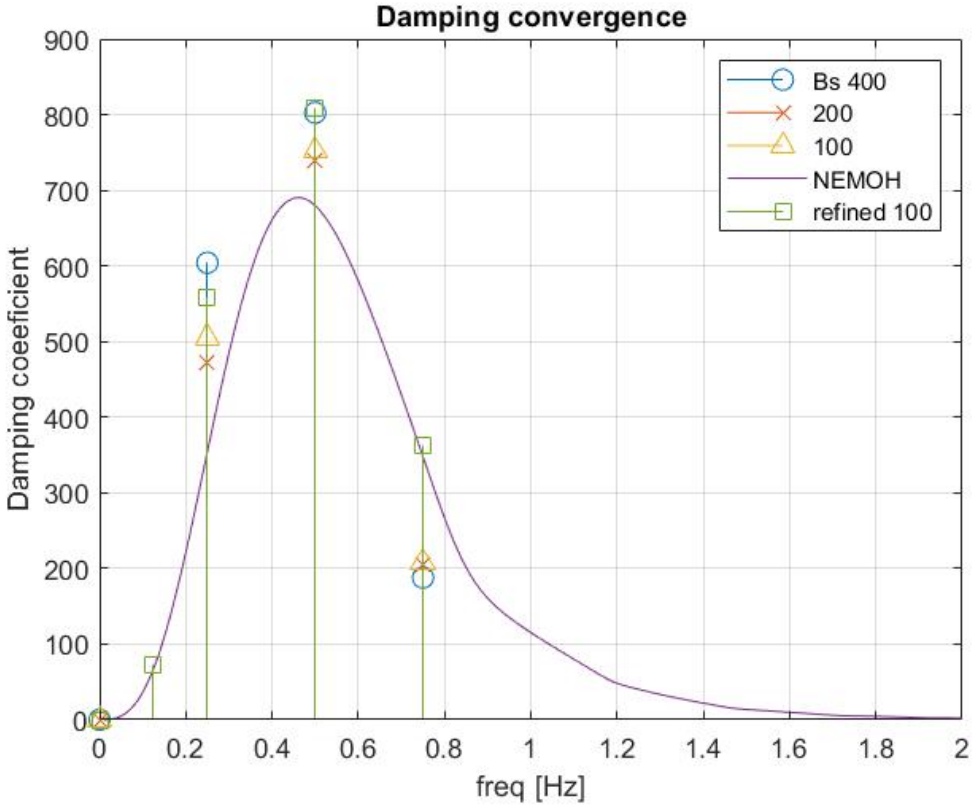

Figure 6.4: Various mixes compared

The damping coefficient obtained from the mix is expected to be identical to the one obtained from the single frequencies. However, frequency analysis is highly sensitive to even the smallest differences, so the slight discrepancies are reasonably considered to be numerical errors, with the red curve being regarded as the valid one.

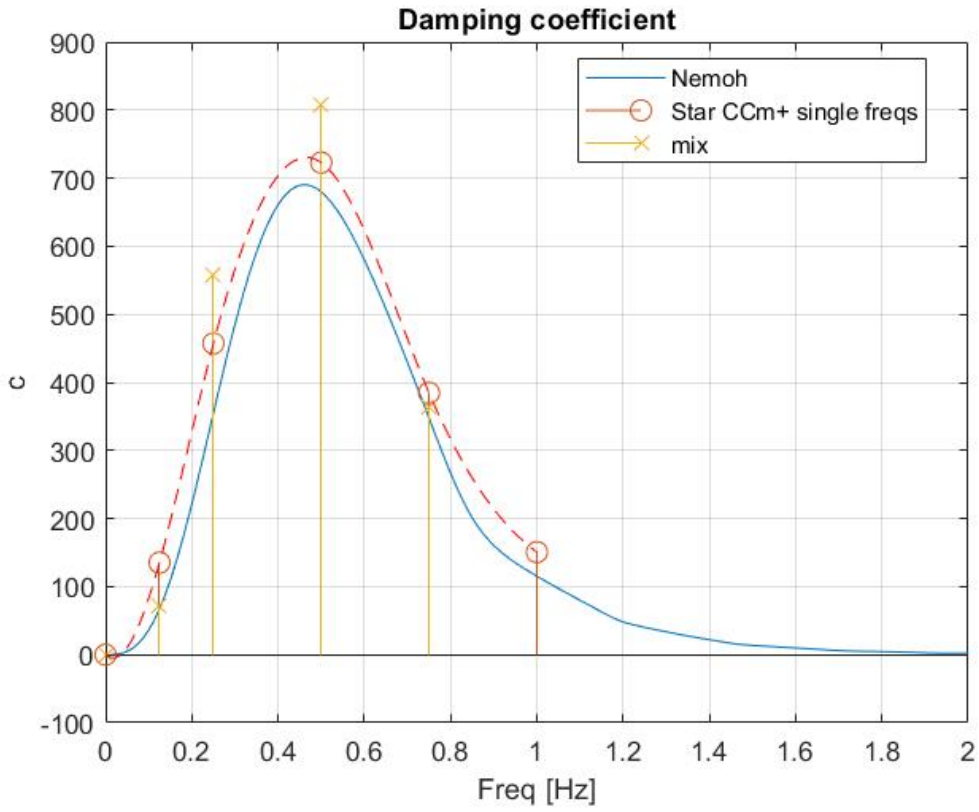

Figure 6.5: Damping comparison between mixed and single frequencies

6.1 Richardson converge analysis

Knowing the exact solution of a certain variable U permits to calculate easily the order of convergence of a CFD simulation: the error 'E' is simply the difference between the result of the simulation and the known exact solution.

$$E = U_{\text{exact}} - U_{\text{cfd}} = Kh^p$$

Where K is a generic constant, h the characteristic dimension of the mesh and p is the order of convergence which can be calculated as:

$$p = \frac{\ln\left(\frac{E_1}{E_2}\right)}{\ln\left(\frac{h_1}{h_2}\right)}$$

So just two simulations would be enough to obtain the convergence order. Obviously the exact solution is not known in this case so other options must be explored

6.1.1 Richardson with theoretical order

If the the theoretical order 'p' of spatial convergence of the simulation, which depends on the flux calculation method used, is known, the error can be estimated starting from that. Two simulations are needed, one with base size h and the other with base size r*h with r>1. Known that:

$$\begin{cases} E_1 = U_h - U_{\text{exact}} = kh^p \\ E_2 = U_{\text{rh}} - U_{\text{exact}} = kr^p h^p \end{cases}$$

The unknown are k and the exact solution, which can be obtained solving the system:

$$U_{\text{exact}} = \frac{r^p U_h - U_{\text{rh}}}{r^p - 1}$$

The error E is then estimated as

$$E_h = (U_{\text{exact}} - U_h) \cdot \text{GCI}$$

where GCI is the Grid Convergence Index, which is often around 3 to be conservative. Considering an order of spatial convergence p=1, this method is applied to the Force 'Fz' comparing every instant with the same time in the other simulation, and then doing the time average of the Errors, involving all samples. Using as the reference size 'h' the simulation with 100, 200 and 400 as base size, here is the plot of the error 6.6.

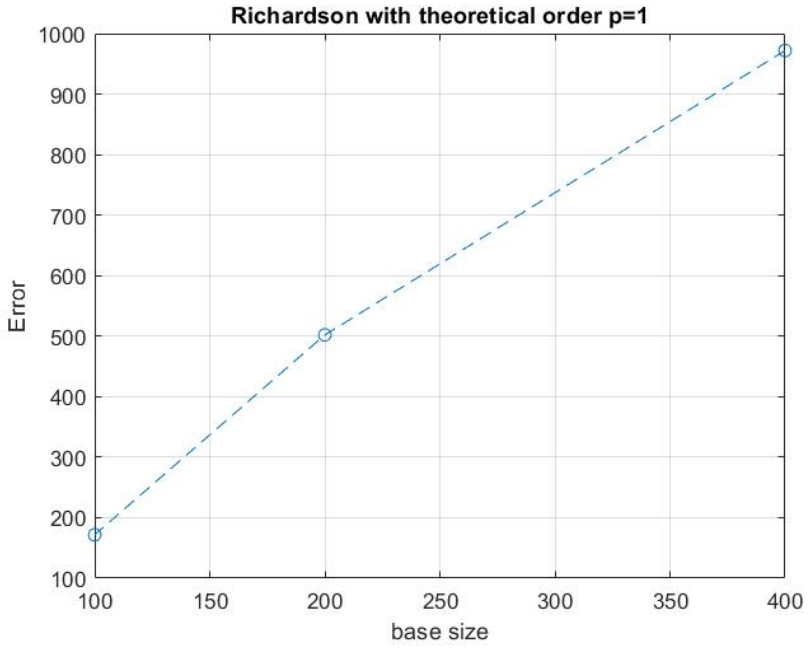

Figure 6.6: Richardson with theoretical order of convergence p=1

The plotted error here is not multiplied for the GCI. Considering that the order of magnitude of the Force is 10^4, the estimated relative error with the smallest base size is less than 2%. As expected the error clearly decreases reducing the base size.

6.1.2 Richardson with effective order

The theoretical order of convergence could be unknown, and even if it is known is only valid for really small meshes, so if two too coarse meshes are considered in this analysis the convergence order will be different. The alternative for this cases is adding a third simulation, with base sizes: h, h2=2*h h3=4*h. The same system of the previous section is written but with a third equation, the effective convergence index is then calculated as:

$$p = \frac{\ln\left(\frac{U_{4h}-U_{2h}}{U_{2h}-U_h}\right)}{\ln 2}$$

and to estimate the exact solution:

$$U_{\text{exact}} = U_h - \frac{U_{2h}-U_h}{2^p-1}$$

Using as reference sizes h=200 and 100 the effective orders equals to p(200)=0.57 and p(100)=0.897, so it's converging to 1, the theoretical order of convergence.

Repeating the same simulation with a base size of 50 would be useful to obtain a third more precise value of 'p', but its computational is prohibitive, so two values will be enough.

Chapter 7

Floating turbine

With the method now validated, it can be applied to a more realistic scenario: a floating wind turbine. The chosen model is the IEA-15-240-RWT, a 15-megawatt (MW) reference wind turbine ([10]) classified as a Class IB direct-drive machine. It features a rotor diameter of 240 meters (m) and a hub height of 150 m (see 7.1). This design is the result of a collaborative effort between the National Renewable Energy Laboratory (NREL), funded by the U.S. Department of Energy, and the Technical University of Denmark (DTU).

Reference wind turbines, such as this one, are open benchmarks with publicly accessible design parameters, serving as standard baselines for research into new technologies and design strategies. They promote collaboration between industry and researchers while safeguarding intellectual property, and they also provide an educational platform for newcomers to understand key design principles and system trade-offs in wind energy. These qualities made it an ideal choice for this thesis.

The envisioned semisubmersible support for this turbine is the UMaine VolturnUS-S Reference Platform ([11]), Designed to accommodate the IEA-15-240-RWT, the system consists of a steel semisubmersible platform with four columns—three radial and one central—and is anchored in place by a three-line chain catenary mooring system. The catenary lines extend radially to anchors positioned 837.60 m from the tower's centerline. The tower is mounted on the central column of the platform, positioning the rotor-nacelle assembly (RNA) at a hub height of 150 m above the still water line (SWL). When installed, the platform has a draft of 20 m and a 15 m freeboard to the upper deck of the columns. The fully assembled system displaces 20206 m^3 of seawater, assuming a density of 1025 kg/m^3.

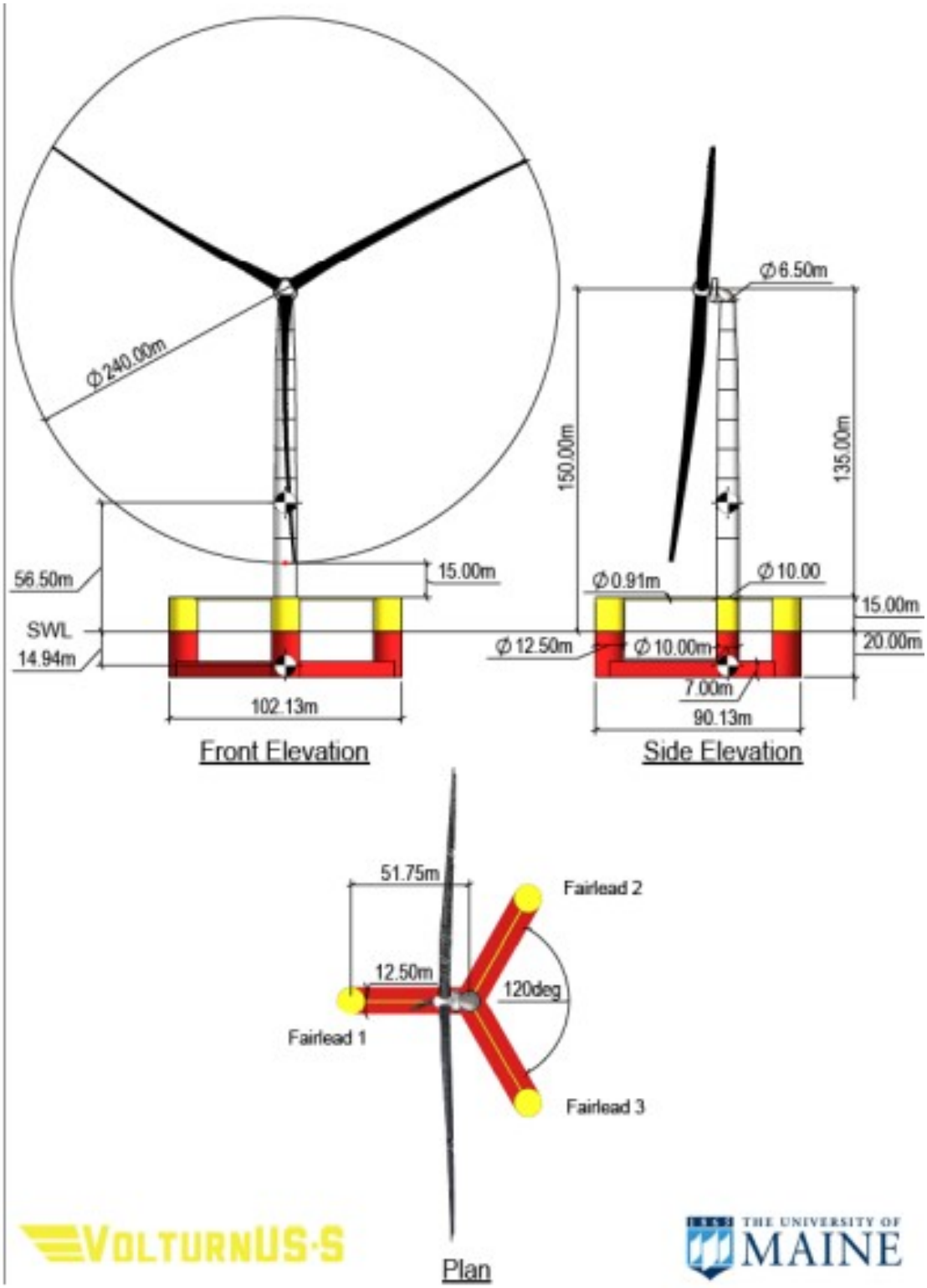

Figure 7.1: General arrangement. Figure courtesy of the University of Maine

Parameter	Units	Value
Turbine Rating	MW	15
Hub Height	m	150
Excursion (Length, Width, Height)	m	90.1, 102.1, 290.0
Platform Type	-	semisubmersible
Freeboard	m	15
Draft	m	20
Total System Mass	t	20,093
Platform Mass	t	17,839
Tower Mass	t	1,263
RNA Mass	t	991
Water Depth	m	200
Mooring System	-	Three-line chain catenary

Table 7.1: General System Properties

7.0.1 Froude scaling

To maintain consistency with the simulation setup used for the sphere, the geometry was scaled down by a factor of 1:70. This rescaling not only reduces computational costs but also makes it possible to physically reproduce the experiment with a prototype matching the size used in the CFD simulations, thereby enabling validation of the numerical results.

To accurately replicate the phenomenon at scale, Froude similarity ([12]) is preserved between the full-sized and scaled geometries. The Froude number (Fr) is a dimensionless parameter employed in fluid dynamics to characterize the flow regime around a body, particularly in open-channel flows and ship hydrodynamics. It is defined as the ratio of inertial forces to gravitational forces in the fluid and indicates whether the flow is dominated by inertia (high Fr) or gravity (low Fr). The Froude number is given by:

$$Fr = \frac{U}{\sqrt{gL}} \tag{7.1}$$

While this approach—commonly used in wave studies—ensures dynamic similarity, it does alter the Reynolds and Weber numbers, potentially introducing differences from the full-scale system. However, in this case, these variations are considered negligible. The scaled properties are reported in 7.2. To follow this approach, the velocities corresponding to the real-size system must be scaled down

Parameter	Units	Scaled Value
Hub Height	m	2.14
Excursion (Length, Width, Height)	m	1.29, 1.46, 4.14
Freeboard	m	0.21
Draft	m	0.29
Total System Mass	kg	58.6
Platform Mass	kg	52.0
Tower Mass	kg	3.68
RNA Mass	kg	2.89
Water Depth	m	2.86

Table 7.2: General System Properties (Scaled 1:70)

by $\sqrt{70}$. For example, an imposed velocity with an amplitude of $A = 0.5\,\mathrm{m/s}$ in the scaled model would represent a real-size amplitude of 15 km/h.

7.1 Comparison BEM-CFD damping

The BEM damping is calculated with NEMOH as done earlier for the sphere. For this test case the damping was also available online ([11]) with another BEM based software called WAMIT, providing the same results. Each simulation is run with a

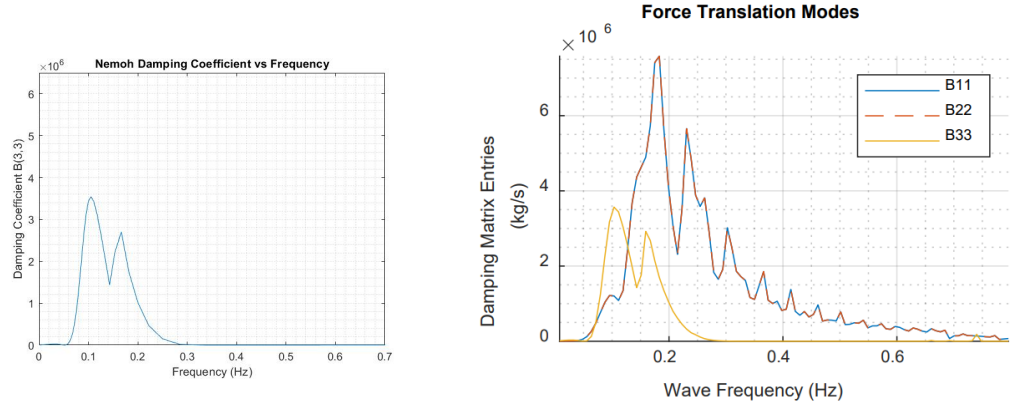

(a) Nemoh Damping Coefficient vs Frequency

(b) Wamit

Figure 7.2: Comparison of Heave damping coefficient

single frequency sinusoidal velocity, ranging from 0.1 to 3 Hz. At least two complete

periods are considered to properly represent the forces in the frequency domain, for example 8.4 is the 1 Hz simulation, the results of the other simulations are available in the image appendix. Some noise is present, but it's neglectable in the frequencies domain, as seen in the FFT plot.

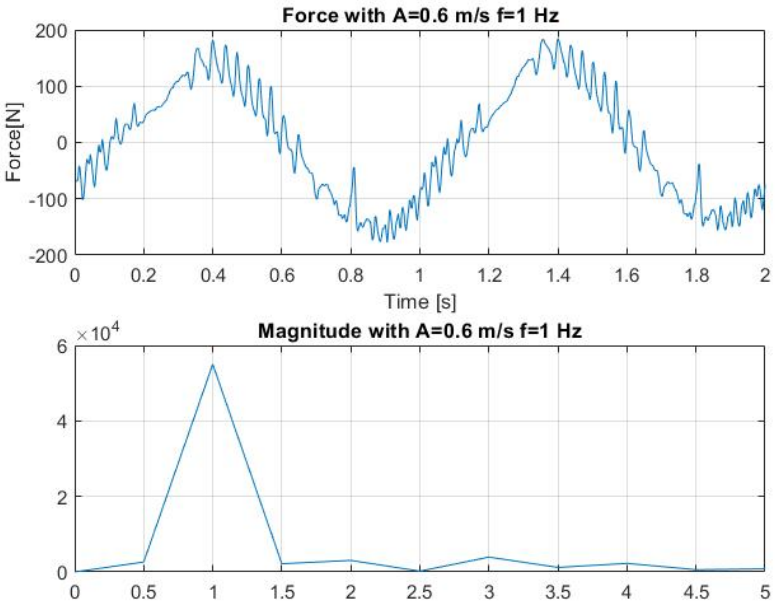

Figure 7.3: f=1 Hz for the substructure 1:70

To properly compare the results obtained from the scaled model to the real size dumping, the scaled forces are multiplied for 70^3 and the velocities for $\sqrt{70}$, while the frequencies need to be divided by $\sqrt{70}$. The damping obtained from the shown simulations (from 8.1 to 8.9) is plotted in figure 7.4.

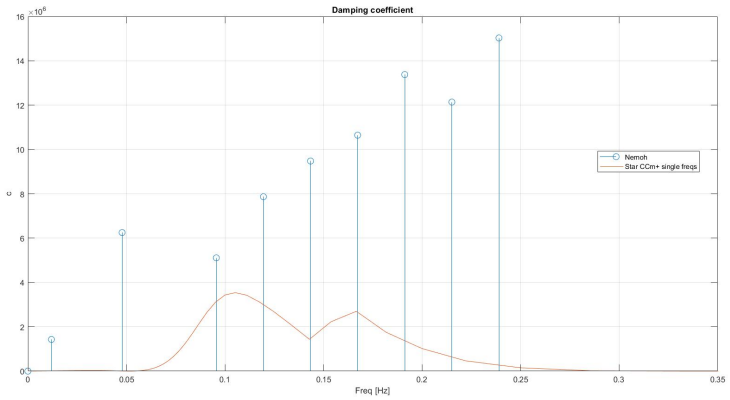

Figure 7.4: Damping comparison for the turbine system

The first noticeable difference is the magnitude of the damping: for the sphere, the geometry was very streamlined and did not produce much vorticity so the two models were really similar. However, here, the arms of the substructure generate a lot of vorticity, leading to an higher damping compared to the BEM. This increase is due to the additional damping caused by the detached boundary layer, resulting in damping that is more than double of the BEM model.

Frequency [Hz]	**Nemoh Damping**	**Star Damping**
0.011952	11173	1.4288e+06
0.047809	4722.9	6.2513e+06
0.095618	3.1144e+06	5.1109e+06
0.11952	3.1115e+06	7.8688e+06
0.14343	1.4346e+06	9.4792e+06
0.16733	2.6986e+06	1.0645e+07
0.19124	1.0193e+06	1.338e+07
0.21514	4.6333e+05	1.2141e+07
0.23905	1.4974e+05	1.5033e+07

Table 7.3: Comparison of Nemoh and Star Damping across different frequencies for the Substructure

For frequencies lower than 0.1 Hz, the BEM model predicts no damping because the structure is designed not to radiate near its natural mode of vibration, which, in this case, is 0.049 Hz for heave. The corresponding frequency to 0.049 Hz in the scaled simulation is around 0.4 Hz (8.2) , that explains the presence of overtones for this test case (spikes in the FFT magnitude for the multiples of the natural

mode), due to the parametric resonance already discussed for the sphere in the previous chapter [9].

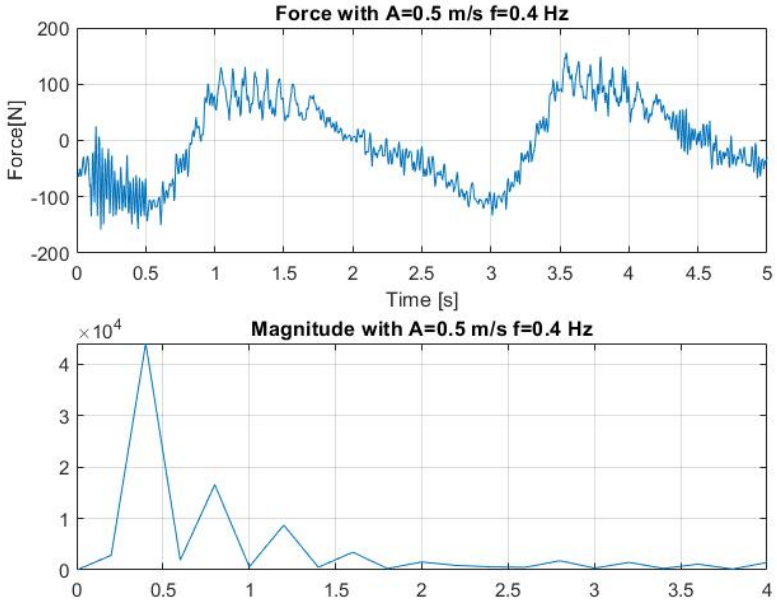

Figure 7.5: f=0.4 Hz for the substructure 1:70

The damping for f<0.05 is produced solely by the vorticity, which explains why the CFD model shows non-zero damping for these low frequencies. In fact, the BEM doesn't work well for plain structures with sharp edges such as the arms of the substructure, the scenes from 7.6 to 7.8 show the chaotic flow field around the structure, while in the same scenes for the sphere 7.9 and 7.10 the flow doesn't produce much vorticity, explaining why the BEM and CFD results are really close.

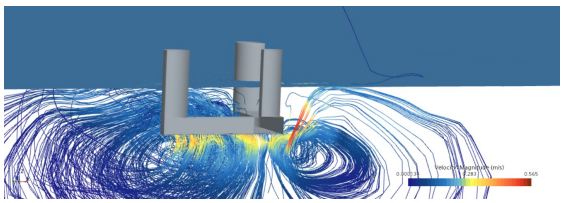

Figure 7.6: Streamlines for the substructure with f=0.1 Hz, A=0.1 m/s after 10.1s

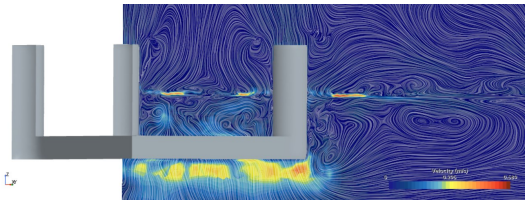

Figure 7.7: Velocity distribution on a plane parallel to the arm for the substructure with f=0.1 Hz, A=0.1 m/s after 10.1s

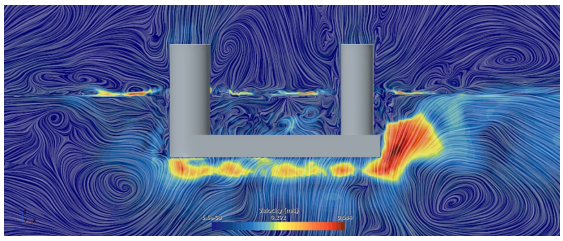

Figure 7.8: Velocity distribution on the plane y=0 for the substructure with f=0.1 Hz, A=0.1 m/s after 10.1s

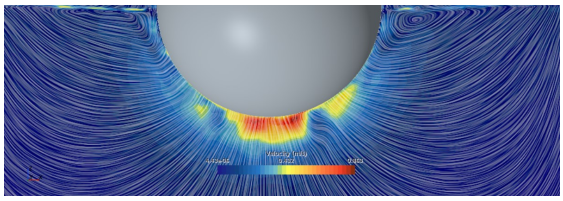

Figure 7.9: velocity field on plane y=0 for the sphere with A=0.5 m/s f=0.5 Hz at t=6 s

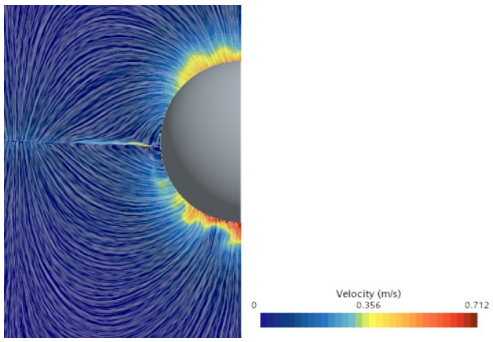

Figure 7.10: velocity field on plane y=0 for the sphere with A=0.5 m/s f=0.5 Hz at t=6 s

The best way to represent the vorticity of a flow field is by analyzing the turbulent kinetic energy (TKE), commonly denoted as k. TKE quantifies the energy contained in turbulent eddies and is expressed as:

$$k = \frac{1}{2}\left(\overline{u'^2} + \overline{v'^2} + \overline{w'^2}\right) \tag{7.2}$$

Here, $\overline{u'^2}$, $\overline{v'^2}$, and $\overline{w'^2}$ are the time-averaged fluctuations of the velocity components in the x-, y-, and z-directions, respectively. Plotted with the same logarithmic scene for both geometries, it's evident that the substructure field 7.11 has a way higher turbulent kinetic energy and in a bigger area with respect to the sphere 7.12, that shows TKE different from zero only in the close proximity of the boundary layer.

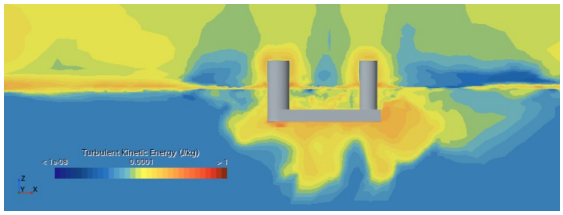

Figure 7.11: TKE scene for the substructure

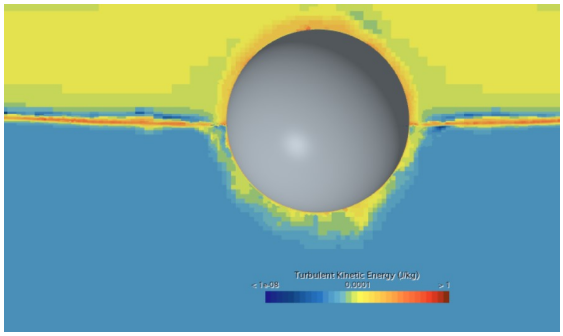

Figure 7.12: TKE scene for the substructure

7.2 Convergence analysis

For this structure, the combined frequencies do not exhibit the same damping behavior as the individual ones, highlighting the system's nonlinearity, as shown in 7.13 . The damping coefficient is higher for the simulation with multiple frequencies, beginning to decay after 0.15 Hz, whereas for the single frequencies, this decay occurs at higher frequencies.

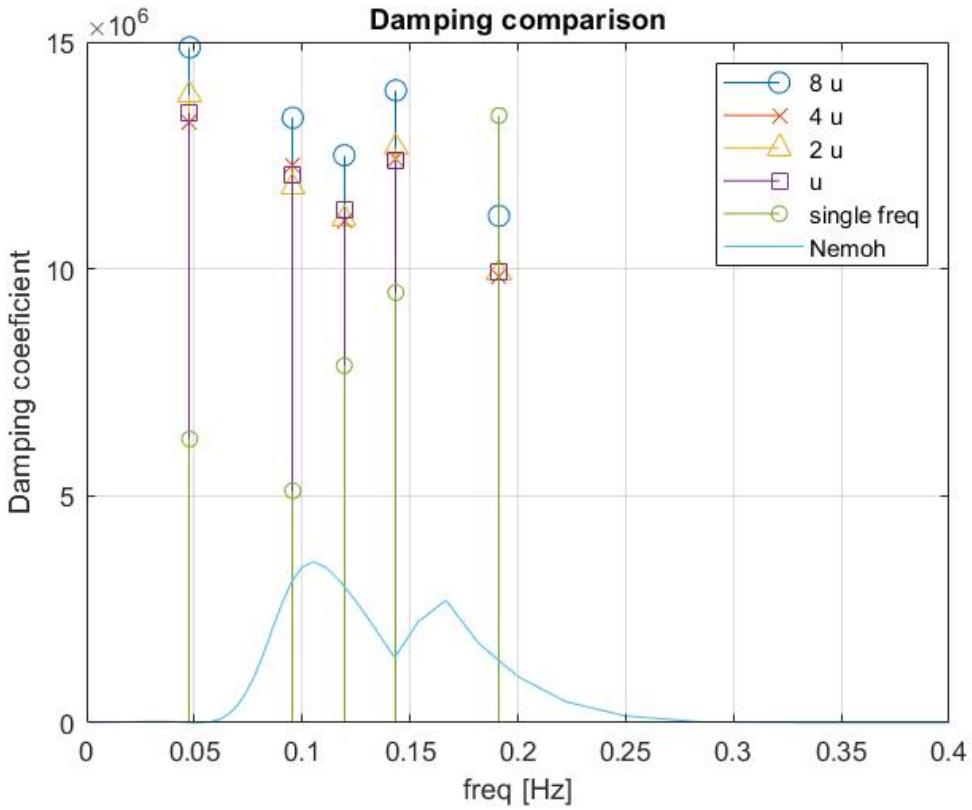

Figure 7.13: Turbine damping comparison for mixed and single frequencies

To analyze grid convergence, the same simulation with an imposed velocity $A\cos(\omega_1 t + \omega_2 t + \omega_3 t + \omega_4 t + \omega_5 t)$ with A=0.5 m/s was repeated, adjusting the target mesh size, with the smallest case corresponding to u=0.001 m. To reduce computational costs in simulations with base sizes of 2u and u, the region of wave refinement was reduced, which led to poorer outcomes: noise oscillations became significantly more prominent in these two cases, suggesting that the actual radiated wave matches the refinement scale used in the 4u simulation.

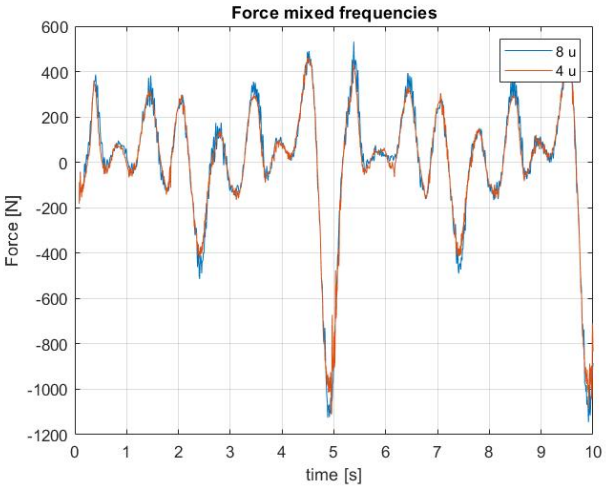

Figure 7.14: Turbine radiated force with target size 8u and 4u

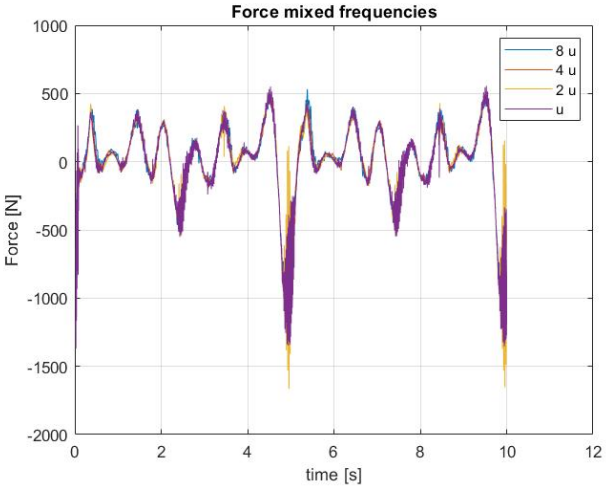

Figure 7.15: Turbine radiated force, underlying the worse results for the last two simulations

As expected, this limited the ability to perform a Richardson convergence analysis, resulting in a negative order of convergence. The logical following step would be repeating the simulations for 2u and u with a larger refinement area. However, the computational time required was prohibitive given the available resources, so this was not pursued, as it fell outside the primary focus of this dissertation.

Chapter 8

Conclusions

To summarize what has been studied in this thesis, the system composed of a floating body is modeled as a mass-spring-damper system, and its heave motion is analyzed. Initially, the damping is obtained based on the potential flow hypothesis, using a computational approach called BEM, with the software NEMOH used for this purpose. The second step involves imposing a sinusoidal velocity in the z-direction on the body and running a RANS simulation in STAR-CCM+. For each imposed frequency, the damping is calculated in the frequency domain as the real part of the ratio of the force and velocity FFTs, where the force is generated by the radiated waves from the floating body.

The comparison was first applied to a simple geometry, a sphere with a 1-meter radius. The two damping values were quite close, with the CFD result being slightly larger.

Once the method was validated, it was applied to study the frequency response of the reference floating substructure UMaine VolturnUS-S, a structure composed of a four-column, three-radial and one central, designed to support the IEA-15-240-RWT wind turbine. In this case, the results were significantly different: the damping obtained via CFD was at least double that of the BEM model. Previous studies ([13]) have shown that drag caused by flow separation constitutes a significant portion of the overall hydrodynamic damping for a floating offshore wind turbine's semisubmersible platform. However, this additional damping effect is not captured by the potential flow model, making it the likely main source of the differences between the damping results from CFD and BEM.

To properly validate the results obtained in this thesis, experimental tests should be conducted for both cases. The goal would have been to introduce a direct correction to the BEM model to account for the overdamping caused by vorticity in the viscous fluid, but more simulations on additional geometries are needed to develop a general correction law.

What can be confidently concluded is that the potential flow model underestimates the damping, and the difference from the real damping increases with the complexity of the structure. The sphere produced little flow separation, so the low computational cost of the BEM approach justifies its use. For the substructure, however, the results were entirely different, indicating that for complex geometries like this, the BEM model is not valid, and a higher fidelity model, such as CFD or experimental data, is required.

8.1 Images appendix

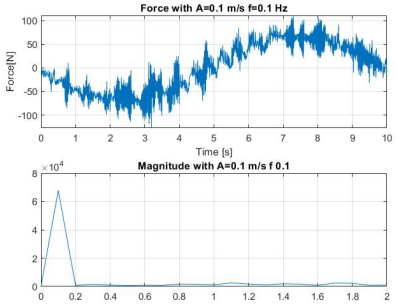

Figure 8.1: f=0.1 Hz for the substructure 1:70

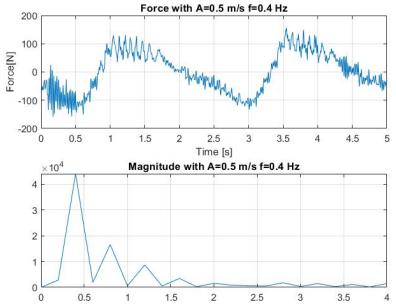

Figure 8.2: f=0.4 Hz for the substructure 1:70

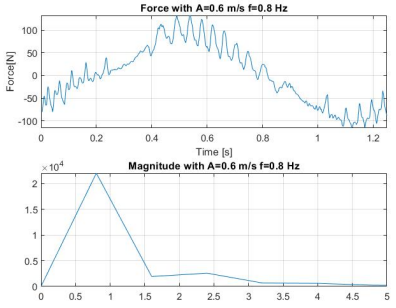

Figure 8.3: f=0.8 Hz for the substructure 1:70

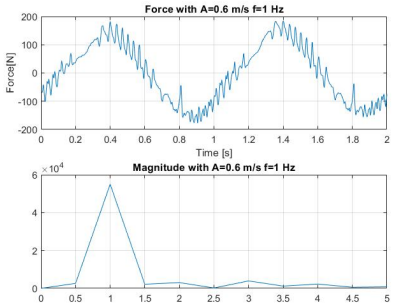

Figure 8.4: f=1 Hz for the substructure 1:70

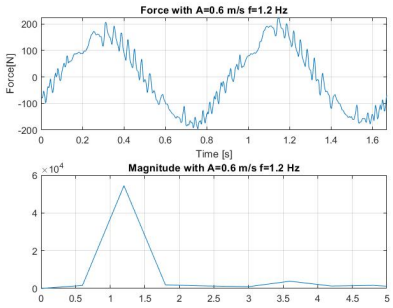

Figure 8.5: f=1.2 Hz for the substructure 1:70

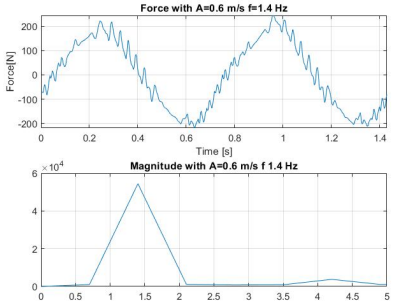

Figure 8.6: f=1.4 Hz for the substructure 1:70

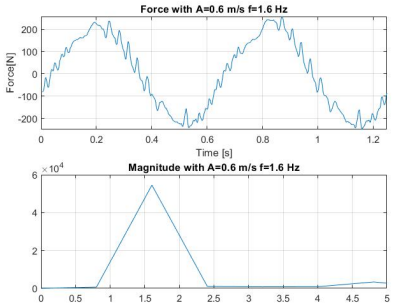

Figure 8.7: f=1.6 Hz for the substructure 1:70

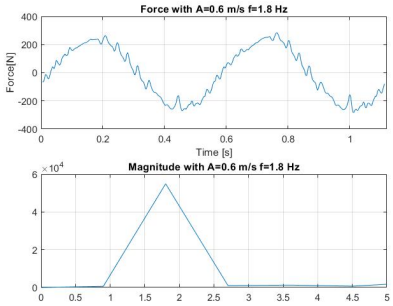

Figure 8.8: f=1.8 Hz for the substructure 1:70

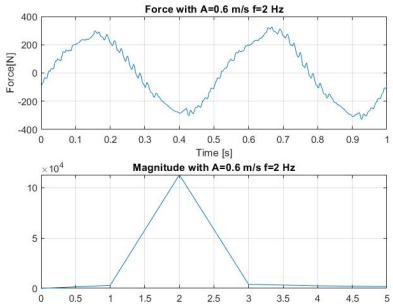

Figure 8.9: f=2 Hz for the substructure 1:70

Bibliography

[1] Piotr Bojek. «International Energy agency report on wind energy». In: (2023) (cit. on p. 2).

[2] John V. Ringwood Markel Penalba Giussepe Giorgi. «Mathematical modelling of wave energy converters: A review of nonlinear approaches». In: (2017) (cit. on pp. 4, 15, 29).

[3] J. J. Monaghan R. A. Gingold. «Smoothed particle hydrodynamics: theory and application to non-spherical stars». In: (1977) (cit. on p. 11).

[4] Liu P. Lin P. *surface tracking methods and their applications to wave hydrodynamics*. Adv Coast Ocean Eng, 1999 (cit. on p. 15).

[5] Visonneau M. Queutey P. «An interface capturing method for free-surface hydrodynamic flows». In: (2007) (cit. on p. 15).

[6] Nichols B. Hirt C. *Volume of fluid (vof) method for the dynamics of free boundaries*. Journal of Computational Physics, 1981 (cit. on p. 16).

[7] David C. Wilcox. *Turbulence Modelling, third edition*. DCW industries, 2006 (cit. on p. 16).

[8] W. E. Cummins. *The Impulse Response Function and Ship Motions*. Hydrodynamics Laboratory, USA, 1962 (cit. on p. 22).

[9] Giuseppe Giorgi et al. «Detecting parametric resonance in a floating oscillating water column device for wave energy conversion: Numerical simulations and validation with physical model tests». In: (2020) (cit. on pp. 35, 50).

[10] Evan Gaertner et al. «Definition of the IEA Wind 15-Megawatt Offshore Reference Wind Turbine». In: (2020) (cit. on p. 44).

[11] Christopher Allen et al. «Definition of the UMaine VolturnUS-S Reference Platform Developed for the IEA Wind 15-Megawatt Offshore Reference Wind Turbine». In: (2020) (cit. on pp. 44, 47).

[12] *Comprehensive Renewable Energy, chapter 8*. 2012 (cit. on p. 46).

[13] Coulling et al. «Validation of a FAST semi-submersible floating wind turbine numerical model with DeepCwind test data». In: (2013) (cit. on p. 55).